1989ApJ...343..323F

THE ASTROPHYSICAL JOURNAL, 343:323–342, 1989 August 1
© 1989. The American Astronomical Society. All rights reserved. Printed in U.S.A.

LATE EMISSION FROM SUPERNOVAE: A WINDOW ON STELLAR NUCLEOSYNTHESIS

CLAES FRANSSON
Stockholm Observatory, Saltsjöbaden, Sweden

AND

ROGER A. CHEVALIER
Department of Astronomy, University of Virginia, Charlottesville

Received 1988 June 27; accepted 1988 December 28

ABSTRACT

Observations of Type Ib and Type II supernovae show strong evidence that the energy input after 100–200 days is dominated by γ-rays from radioactive decay of ^{56}Co. The energy deposition of these γ-rays, and the subsequent thermalization of the nonthermal electrons, are calculated using Monte Carlo techniques. The relative fractions going into heating, ionizations, and direct excitations are studied. Above an electron fraction of ~ 0.1 direct excitations are negligible, and the line emission arises from thermal processes. The temperature and ionization structure of the ejecta and its emission are discussed for general cases, and for detailed nucleosynthesis models. It is found that the emission is dominated by neutral and singly ionized lines, the strongest due to [O I], [Ca II], Mg I], [C I] and [Si I]. Tests of the explosion models and determinations of absolute and relative abundances from the late emission are studied. For a given model, the relative and absolute line strengths depend on both the column densities of the different abundance zones, *and* the relative abundances *within* each zone. For reliable modeling, the density structure must be known. It is shown how the emission-line profiles can be used as a powerful diagnostic of this, as well as of the abundance structure of the ejecta. The variation of the composition with the He core mass is shown to lead to substantial differences in the spectra, especially in the [O I]/[Ca II] emission-line ratio. Also, the degree of convective mixing is important for the result. The late spectrum is thus a good diagnostic of the nucleosynthetic structure of the supernova. At late times, a thermal instability is possible, since fine-structure far-IR lines dominate the cooling. This may trigger molecule and dust formation in the ejecta. The emission from a central pulsar may prevent this from occurring.

The model is applied to the observations of the Type Ib SN 1985F. From a nebular analysis, including most of the diagnostic lines available, it is concluded that a white dwarf model cannot be excluded, purely on this basis. However, from calculations of the emission from 4–8 $M_\odot$ He cores, it is found that a core mass of ~ 8 $M_\odot$ reproduces both the total and the relative line strengths well, while lower mass cores give a considerably poorer agreement. Thus, the spectrum indicates that the Type Ib supernovae come from stars of ~ 25 $M_\odot$ and above. The density distribution, as inferred from the line profiles, is, however, considerably more extended than in the hydrodynamical models. This may be a result of instabilities. A macroscopic mixing of clumps from the different burning shells is shown to be the most likely explanation for the lack of a velocity correlation from lines of the different elements. Models based on exploding white dwarfs are shown to be inconsistent with the observations, owing to low absolute line luminosities and to the strong [C I] lines.

Subject headings: γ-rays: general — nucleosynthesis — stars: interiors — stars: supernovae

I. INTRODUCTION

Although supernovae are thought to be the dominant sources of heavy elements in the universe, the direct evidence for heavy-element ejection in supernovae has been scarce. One problem is that near maximum light (the first 100 days) most of the expanding gas is optically thick at optical wavelengths. For Type II supernovae this means that only the hydrogen envelope is observed at early times. For Type Ia supernovae, the outer layers are heavy-element–rich and there has been progress in relating the observed spectra to thermonuclear models (Branch *et al.* 1985). However, the stellar atmosphere problem is complex and it has still not been solved in detail. The interpretation of late (age more than ~ 200 days) observations of supernovae is of particular interest from two points of view. First, most of the gas is optically thin, except in resonance lines. This simplifies the analysis of the physical conditions in the expanding gas. Second, the inner layers are subject to direct observation. There has already been substantial success in the interpretation of the late spectra of Type Ia supernovae. The studies of Meyerott (1980) and Axelrod (1980*a*, *b*) have provided strong evidence for the ejection of 0.5–1 $M_\odot$ of Fe in the explosion of a Type Ia supernovae. This evidence favors models for Type Ia supernovae in which they are the thermonuclear explosion of a white dwarf and derive their radiative energy from radioactive energy input.

High-quality observations of Type II supernovae at late times have been lacking because of the faintness of the emission. Good optical spectra are only now becoming available (e.g., Uomoto and Kirshner 1986 on SN 1980K; Filippenko 1988 on SN 1986I). In this respect SN 1987A is, of course, the most spectacular case. Apart from SN 1987A, the best data are available on the late emission from Type Ib supernovae. The object SN 1985F was intensively studied by Filippenko and Sargent (1985, 1986), and it subsequently became clear that this supernova is of Type Ib by comparison with late spectra of SN 1983N (Gaskell *et al.* 1986) and SN 1984L (Schlegel and Kirshner 1989). The late spectra are dominated by oxygen lines, whereas the late spectra of Type Ia supernovae are domi-

© American Astronomical Society • Provided by the NASA Astrophysics Data System

1989ApJ...343..323F

nated by iron lines (Kirshner and Oke 1975; Branch 1984). The implication is that the elemental compositions of these two types of events are different.

The purpose of the present paper is to discuss the basic physics going into models of the late spectra of core-collapse supernovae. We have already applied these models to Type II supernovae, in particular SN 1987A (Fransson and Chevalier 1987; Fransson 1987, 1988). In this paper we will discuss the basic physics going into this type of calculation and the application to Type Ib's. Our models assume that the basic energy source for the radiation is the radioactive decay of ^{56}Co. There are both observational (Wheeler and Levreault 1985; Begelman and Sarazin 1986) and theoretical (Woosley and Weaver 1986) reasons to believe this. Our paper is arranged as follows. The physical processes relevant to the late emission are described in § II, and qualitative results based on these processes are given in § III. The relation between gas emissivities and spectral line profiles is discussed in § IV. Detailed models are presented in § V, and the results are applied to late Type Ib spectra in § VI. Conclusions are given in § VII.

II. PHYSICAL PROCESSES

a) Energy Deposition by γ-Rays

At the supernovae ages considered here, the dominant energy source is the radioactive decay of ^{56}Co. Energy deposition by the γ-rays has already been examined in the context of Type Ia supernovae. Colgate, Petschek, and Kriese (1980) presented results for the total γ-ray deposition in a uniform sphere in which the source isotopes are uniformly distributed. Axelrod (1980*b*) calculated the deposition function for a particular exploding white dwarf model at several stages of evolution (see also Weaver, Axelrod, and Woosley 1980). He found that the total deposition function was quite close to that of Colgate, Petschek, and Kriese (1980), within about 20%. The white dwarf deposition calculation was used to define an effective deposition " opacity " for use in a variety of white dwarf explosion calculations. Woosley, Taam, and Weaver (1986) used this " opacity " in the analytic calculation of light curves for helium detonation supernovae. Sutherland and Wheeler (1984) also treated γ-ray deposition with an effective " opacity," but they did consider the detailed geometry of the γ-ray source distribution. Their approximation was to treat the γ-ray scattering as an absorption process.

In this section we reexamine the energy deposition by γ-rays from ^{56}Co decays. The reasons for doing this are that we require the energy deposition as a function of radius in order to model emission-line profiles, and that the cases studied here may have a central source, as opposed to a distributed energy source. At the γ-ray energies of interest, the photons interact with matter primarily through incoherent electron scattering. We follow the energy losses of individual photons by a Monte Carlo technique (Cashwell and Everett 1959). We assume that the gas has $Z/A = 0.5$, where Z is the number of electrons per atom and A is the atomic mass in atomic mass units.

We examined the total energy deposition as a function of depth for four cases, which are illustrated in Figure 1. The cases are (1) uniform energy deposition throughout a uniform sphere, (2) central energy deposition in a uniform sphere, (3) uniform deposition throughout a uniform shell with a ratio of inner to outer radius $R_i/R_o = 0.8$, and (4) deposition at the inner edge of a uniform shell with $R_i/R_o = 0.8$. These cases are intended to illustrate the effects of the geometry of the absorbing gas as well as the effects of the distribution of the energy source. Case 1 is the same as that calculated by Colgate, Petschek, and Kriese (1980), and our results agree with theirs to within 9%. The results are very close for low values of the effective optical depth; the slight deviations occur at intermediate values of this parameter.

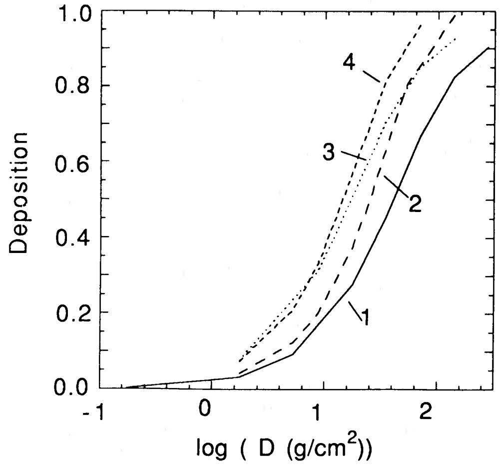

FIG. 1.—Total energy deposition of the ^{56}Co γ-rays as a function of the column density, D, for different geometries: (1) Uniform distribution of sources in a sphere. (2) Central source in a sphere. (3) Uniform source distribution throughout a shell of radii $R_i/R_o = 0.8$. (4) Source at inner edge of a shell with $R_i/R_o = 0.8$. In all cases, the density is uniform.

The general form of each curve in Figure 1 can be roughly fitted by a curve of the form $1 - \exp(-D\kappa_\gamma)$, where D is the column density out from the center of the mass distribution and κ_γ is the effective deposition " opacity " for the γ-rays. Estimates of κ_γ determined in this way give $\kappa_\gamma = 0.017$, 0.027, 0.038, and 0.046 cm^2 g^{-1} for cases 1–4 respectively. The exponential gives a better fit to the cases with a central energy source (cases 2 and 4) than to the cases with a distributed source. At low D, the value for case 2 is applicable to any density distribution with a central energy source. The other cases depend on the geometry of the energy-source distribution. For the exploding white dwarf case, Woosley, Taam, and Weaver (1986) found $\kappa_\gamma \approx 0.07$ cm^2 g^{-1}. Their density distribution did have a steep outer gradient, but much of the mass was in a central region with slowly varying density.

The energy deposition as a function of radius, $\epsilon_\gamma(r)$, is particularly sensitive to the distribution of the energy source. For small values of D (i.e., single scattering) and a central energy source, $\epsilon_\gamma(r)$ is easy to calculate. If the density distribution is a uniform, we have

$$\epsilon_\gamma(r) \propto \frac{1}{r^2} . \tag{1}$$

For the case of uniform energy input in a uniform sphere at low D, an integration over the source distribution yields

$$\epsilon_\gamma(r) \propto \left[1 + \frac{1 - x^2}{2x} \ln \left(\frac{1 + x}{1 - x} \right) \right] . \tag{2}$$

where $x = r/R_o$. This distribution is relatively uniform. In the limit of large D, the distribution becomes completely uniform. With a central energy source, the deposition, f, becomes more centrally concentrated at large D. If $\tau_\gamma = D\kappa_\gamma$ Figure 2 shows the differential deposition, $df/d\tau_\gamma$, as a function of depth in a sphere with τ_γ up to 3.8. The deposition in spheres with smaller

© American Astronomical Society • Provided by the NASA Astrophysics Data System

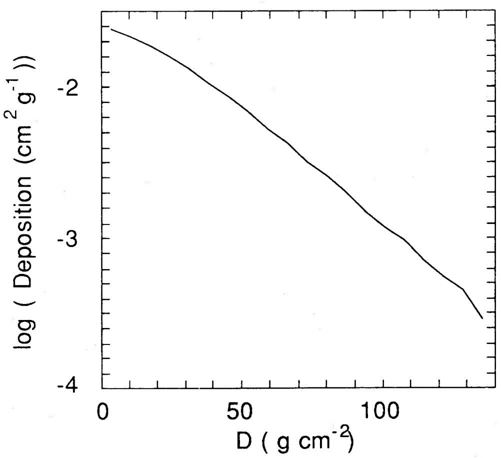

FIG. 2.—Differential energy deposition in γ-rays, df/dD, as a function of the column density, D, for a uniform sphere with a central source of γ-rays.

total depths is quite well approximated by this curve. If the energy deposition could be approximated by an absorption process (e.g., Sutherland and Wheeler 1984), the curve in Figure 2 would be a straight line. The curvature is due to the fact that scattered photons in the outer parts of the sphere have a greater probability of escape.

b) *Nonthermal Electron Losses*

The energetic 0.1–1 MeV electrons created by the Compton scattering will lose their energy in ionization and excitation of discrete levels of neutral and singly ionized atoms. In addition, they will slow down by Coulomb scattering off thermal free electrons ($kT < 1$ eV). The stopping distance, D_e, for a fast electron in a neutral medium has been calculated by Rohrlich and Carlson (1954), including relativistic effects. At low energy ($v/c \ll 1$) one finds that D_e is given by

$$D_e \equiv \frac{AE}{Z(dE/dx)} \approx \frac{0.307}{\beta^2}\left[\ln\left(\frac{E}{I'}\right)+\frac{1}{2}\right] \text{ g cm}^{-2} , \qquad (3)$$

where $A/Z \approx 2$, $\beta = v/c$ and I' is the effective ionization potential, including effects of both excitation and ionization. For oxygen $I' \approx 91$ eV (Ahlen 1980). Thus, D_e decreases rapidly with energy; at 1 MeV we find (from the exact expression) that $D_e = 0.62$ g cm^{-2}, and at 0.5 MeV, $D_e = 0.28$ g cm^{-2}. The γ-ray mean free path corresponds to $D \approx 33$ g cm^{-2}, so only if the total γ-ray optical depth is less than 0.02 will the energetic electrons escape the remnant. If there is a nonradial magnetic field, the stopping distance will be even smaller (Colgate and McKee 1969; Axelrod 1980*b*). In the following we thus consider the nonthermal electron energy deposition as a local process.

To calculate the structure of the supernova, we are interested not only in the total energy deposition but also in the relative fractions going into ionizations, excitations, and heating of the thermal electrons. The situation is further complicated by the fact that the secondary electrons, produced by the ionization, will give rise to additional ionizations and excitations. This cascade was discussed earlier for hydrogen-dominated plasmas by Spitzer and Tomasko (1968), Spitzer and Scott (1969), and Shull (1979). In the supernova case the situation is different, with the inner region dominated by oxygen, helium, and other heavy elements. We have therefore calculated the energy deposition using the Monte Carlo method along the lines of Shull (1979). In order to be able to take the fate of the secondaries into account, we start the calculation at low energy, so that the relative deposition of the secondary electrons produced which, of course, have a lower energy than the original electron) is already known. In this way we can finally determine the deposition of the primary electrons created by the γ-rays. The cross sections and secondary electron distributions used are given in Appendix A.

The relative fraction of the energy given to the free, thermal electrons and that going into ionizations and excitations depends on the free-electron fraction, $x_e = n_e/n_{\text{tot}}$, and hence on the state of ionization, of the different elements. Here n_{tot} is the number density of ions plus neutral atoms. In most of the core, oxygen has a much higher abundance than the other elements, and we can make the approximation that the electron fraction is determined by the ionization equilibrium of O I, O II, and O III. Oxygen thus plays the same role as hydrogen for ordinary cosmic abundances, and the result is thus determined only by one parameter, x_e. For the other "trace ions" the energy going into ionizations of the respective elements will then be proportional to their abundances. In the other regions (the He shell and the Si shell) we have made analogous approximations.

In Figure 3 we show the result of our calculations for oxygen as a function of the electron fraction. The most interesting feature is the increase of the energy going into the free electrons and the decrease of that going into direct excitations, as x_e increases. This is mainly a result of the larger effective cross section for electron scattering of the low-energy secondary electrons, whereas the high-energy primaries deposit most of their energy into ionizations. Therefore, the decrease in excitations is considerably larger than that of ionizations. Above $x_e \sim 0.1$ the energy going into excitations is less than 3%, and we can neglect it compared with that going into ionizations and electron heating. This conclusion is in contrast to, e.g., aurorae, where $x_e \approx 10^{-4}$ and one can neglect the electron heating. As a check of our calculations, we have compared our results with those of Dalgarno and Lejeune (1971) for $x_e < 0.01$, and find good agreement in the ionization and heating efficiency, although the energy going into the different excited levels in some cases differ considerably. This is probably due to our use of more recent atomic data. At $x_e = 0.1$, for the direct

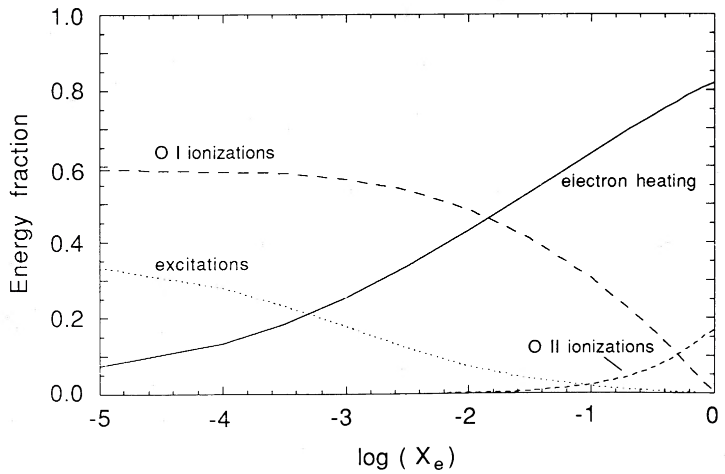

FIG. 3.—Relative fractions of the total deposited energy going into ionizations, excitations, and heating of the thermal electrons for O I.

© American Astronomical Society • Provided by the NASA Astrophysics Data System

1989ApJ...343..323F

excitations 37% of the energy went into the $3s\ ^3S$ level, 28% into $3s\ ^3P$, 25% into $3p\ ^3D$, 6% into the $2p\ ^1D$ level, and 1.3% into the $2p\ ^1S$ level. For the other elements we neglect direct excitations. It is convenient to define an effective ionization potential χ_i so that the number of ionizations of the ion i per unit time is given by

$$R_i = 4\pi \frac{J_\gamma \sigma_\gamma}{\chi_i} n_i \, , \tag{4}$$

where J_γ is the mean intensity of γ-rays and $\sigma_\gamma = A_i m_p \kappa_\gamma$ is the effective cross section for the γ-rays on the ion i with atomic weight A_i. For a point source of γ-rays and no absorption, $J_\gamma = L_\gamma / 16\pi^2 r^2$. L_γ is the γ-ray luminosity given by $L_\gamma = 1.36 \times 10^{43} [M(^{56}\mathrm{Ni})/M_\odot] e^{-t/114 \text{ days}}$ ergs s^{-1}.

A general property of these calculations is that the deposition is not sensitive to the initial energy of the primary electrons as long as this is more than about 10 keV, in agreement with the results found by Shull (1979) for hydrogen. This simplifies the calculations, since the spectrum of the primary electrons varies with distance from the source if the gas is optically thick to the γ-rays. The exact shape of the γ-ray spectrum is therefore also unimportant.

c) Thermal and Ionization Balance

In the cases considered in this paper the ionization of the gas is dominated by the γ-ray absorption and subsequent ionizations by the nonthermal electrons, but in some cases radiative ionization may also be important. The ionization equilibrium between ions i and $i + 1$ is therefore given by

$$\left(4\pi \frac{J_\gamma \sigma_\gamma}{\chi_i} + 4\pi \int_{\nu_0}^{\infty} \frac{J_\nu \sigma_\nu}{h\nu} d\nu + C_i n_e + \sum_k \zeta_{k,i} n_k\right) n_i = \left(\alpha_{i+1} n_e + \sum_k \zeta_{k,i} n_k\right) n_{i+1} \, , \tag{5}$$

where J_ν is the mean intensity of the radiation, σ_ν the photoionization cross section, ν_0 the threshold frequency, C_i the collisional ionization rate by thermal electrons, α_{i+1} the recombination coefficient, and $\zeta_{k,i}$ the charge transfer rate between ions k and i. J_ν includes both the direct ionizing radiation from the photosphere of the supernova, and the diffuse emission by the gas.

Neglecting for the moment all ionizing processes other than the γ-ray ionization, as well as recombination due to charge transfer, it is seen that the ionization balance depends only on the ratio $4\pi J_\gamma / \chi_i n_e \alpha_{i+1}$. In analogy to, e.g., photoionization models for QSO emission-line regions, it is therefore useful to define a parameter Γ_γ characterizing the state of ionization by

$$\Gamma_\gamma = \frac{4\pi J_\gamma}{c n \chi_i} \equiv \frac{n_\gamma}{n} \, , \tag{6}$$

where n_γ is the effective number density of ionizing γ-rays. In the calculations we have included thermal collisional ionization mainly for completeness, since it is seldom important at the low temperatures considered here. Photoionization by the diffuse emission from the gas (mainly O I recombination emission) is, however, very important for some ions with low ionization potentials, such as Mg I, Ca I, and Na I. Charge transfer with various ions can be important both as an ionizing and as a recombination process. Unfortunately, little experimental and theoretical work for the relevant ions and energies is available. This may affect the result by a large factor in some cases, since the rates often exceed 10^{-10} cm^3 s^{-1}, compared with radiative recombination rates of 10^{-13} to 10^{-12} cm^3 s^{-1}. To be effective, however, the abundance of the relevant ion k has to be larger than $\sim \alpha_{i+1}/x_e \zeta_{k,i+1} \sim 10^{-3}$ to 10^{-4}. The recombination includes both radiative and dielectronic recombination, although the latter is usually slow at the low temperatures encountered here.

The continuum intensity is calculated for each frequency by solving the equation of transfer along lines of constant impact parameter for both the outgoing and the ingoing radiation (see, e.g., Nordlund 1984). For the formal solution of the equation of transfer a recursive method due to Scharmer (1987) has been used. The solution then proceeeds as a lambda iteration, which converges fast, since the important sources of emission are determined by the nonthermal input, i.e., decoupled from the radiation field itself. In the calculation of the diffuse emission, we include all lines and continuum processes of importance. In particular, the recombination emission from the resonance lines of O I is important to include as an ionizing source. The line transfer is solved using the Sobolev approximation, which is well suited to our purposes. The continuum absorption of the line emission is included, using the modification of the Sobolev method by Hummer and Rybicki (1985).

The main heating source is the energy input of the γ-rays to the thermal electrons, which is calculated in the way described in § II*b*. In addition, there is also a minor contribution due to photoionization by the diffuse radiation. Most of the cooling is due to collisional excitation of lines from neutral and once-ionized elements. The elements included are He, C, N, O, Ne, Na, Mg, Si, S, Ar, Ca, and Fe. For all elements we include at least the first two ionization stages. In contrast to Axelrod (1980*a*, *b*), who, however, included only Fe and Co, we do not calculate the line emission of Fe and Co in detail. This is reasonable for massive stars, where most of the emission is dominated by the lighter elements. Neither do we include hydrogen, since we are interested primarily in the emission from the region where nuclear processing has taken place. This has to be kept in mind when comparing our models with Type II's. A one-zone model of the hydrogen envelope with only Lyα, [O I] $\lambda\lambda$6300, 6364, and Mg II λ2800 is discussed by Chugai (1988). For the forbidden lines we solve the level populations for a three-level atom, whereas resonance lines and semiforbidden lines are treated as two-level atoms, taking collisional and radiative processes into account. Since the forbidden lines may be optically thick under certain conditions, we solve for the level populations by iterations, starting from the thin case. Recombination cooling and free-free cooling are also included. O I, He I, and Ca II are treated as multilevel atoms, since many of the interesting levels are strongly coupled and also optically thick. For O I we use a nine-level atom plus the ground states of O II and O III, shown in Figure 4. Both collisional and radiative bound-bound transitions are taken into account, including scattering of any background radiation from the photosphere. Photoionization and collisional ionization are included for the excited levels. The He I atom consists of 12 levels, including the three lowest singlet levels and triplet levels up to $4\ ^3F$. In the same way, for Ca II we include the ground state and the excited states $3d\ ^2D$ and $4p\ ^2P$, which are coupled by the H and K lines, the triplet ^2D–^3P, $\lambda\lambda$8542, 8662, 8498 and the forbidden ^2S–^2D, $\lambda\lambda$7291, 7324. At the low temperatures sometimes encountered at late epochs ($T_e \leq 3000$ K), cooling by fine-structure transitions of C I, C II, O I, Ne II, Si I,

© American Astronomical Society • Provided by the NASA Astrophysics Data System

1989ApJ...343..323F

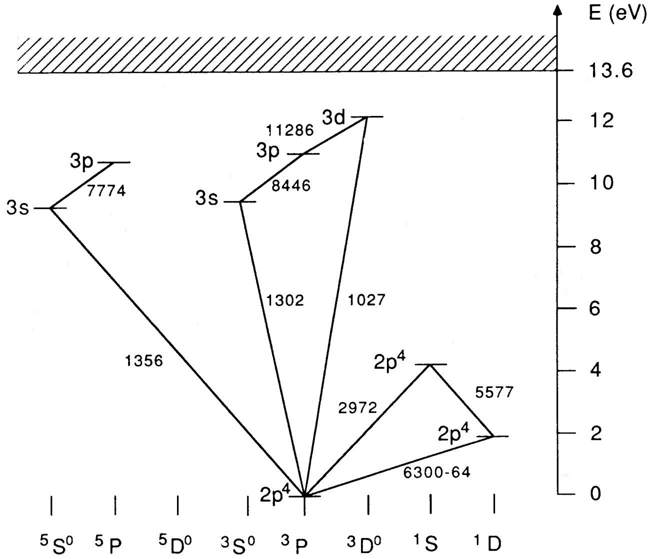

FIG. 4.—Grotrian diagram for the levels and transitions included in the model atom of O I.

Si II, S II, Ar II, Fe I, II can be important. These are calculated taking two or three levels into account.

III. QUALITATIVE RESULTS

Many of the main features of these oxygen-dominated models can be understood from an analysis of a simplified model. In this section we discuss the simple case of a pure oxygen remnant powered by a point source of γ-rays.

Since the most important parameters are the oxygen core mass, $M_{\rm core}$, the core velocity, $V_{\rm core}$, and the ^{56}Ni mass, $M(^{56}\mathrm{Ni})$, it is of interest to discuss the typical range of these. By the oxygen core (and similarly with the He core) we understand the whole region interior to the oxygen burning shell, i.e., including, e.g., the Si shell, but not the compact remnant in the center. The O core mass is fairly well determined from theoretical calculations (Woosley and Weaver 1987, hereafter WW) and is insensitive to mass loss of the progenitor. For a 15 $M_\odot$ ZAMS star Woosley and Weaver find an O core mass of 1.06 $M_\odot$; for 25 $M_\odot$, they find 3.65 $M_\odot$, and for 35 $M_\odot$, 9.65 $M_\odot$ (all excluding the neutron star). The core velocity is, however, sensitive to the degree of mass loss, and this will be discussed in § V*a*. Depending on the envelope mass and the explosion energy, the likely range of velocities is $\sim$1000–5000 km s^{-1}. As for the ^{56}Ni mass, the theoretical values are sensitive to the mass cut, but are in general 0.05–0.3 $M_\odot$, increasing with the core mass (Woosley and Weaver 1986). The late light curves of several Type II and Type Ib supernovae are most likely powered by radioactivity (Barbon, Cappellaro, and Turatto 1984). From the photometry of SN 1979C (Barbon, Ciatti, and Rosino 1982) and SN 1980K (Barbon *et al.* 1982) we estimate that both these supernovae produced $0.06[H_0/(50\ \mathrm{km\ s^{-1}\ Mpc^{-1}})]^{-2}\ M_\odot$ of ^{56}Ni. For this we have used a reddening $E_{B-V} = 0.13$ and 0.30, respectively, and standard bolometric corrections based on the $B-V$ colors. For SN 1987A the best fit gives 0.075 $M_\odot$ (e.g., Nomoto, Shigeyama, and Hashimoto 1987; Woosley 1988). The bolometric light curve of the Type Ib SN 1983N gave $0.3[\mathrm{H}_0/(50\ \mathrm{km\ s^{-1}\ Mpc^{-1}})]^{-2}\ M_\odot$, assuming $E_{B-V} = 0.16$ (Panagia *et al.* 1989).

If the gas is assumed to be optically thin to the γ-rays and charge exchange reactions with other species are neglected, the state of ionization is completely determined by the γ-ray ionization parameter Γ_γ (§ II*c*). Using a typical value of $\chi_i = 30$ eV, we obtain for a uniform-density gas dominated by oxygen

$$\Gamma_\gamma = 18.2\left[\frac{M(^{56}\mathrm{Ni})}{0.1\ M_\odot}\right]\left(\frac{V_{\rm core}}{5000\ \mathrm{km\ s^{-1}}}\right)\left(\frac{M_{\rm core}}{1\ M_\odot}\right)^{-1}\left(\frac{t}{100\ \mathrm{days}}\right)e^{-t/114\ \mathrm{days}}\,. \qquad (7)$$

The cooling is dominated by forbidden lines of O I and O II. Since the characteristic density of the supernova is

$$n = \frac{3M}{4\pi m_p A R^3} = 2.2\times 10^8\left(\frac{M_{\rm core}}{1\ M_\odot}\right)\left(\frac{V_{\rm core}}{5000\ \mathrm{km\ s^{-1}}}\right)^{-3}\left(\frac{t}{100\ \mathrm{days}}\right)^{-3}\ \mathrm{cm^{-3}} \qquad (8)$$

(where A is the mean atomic weight ≈ 16) and thus $n_e \sim 10^6$–10^8 cm^{-3}, collisional de-excitation is important, and the cooling thus depends on the density. The resulting temperature is therefore characterized by two parameters, Γ_γ and n. In Figure 5 we show the ionization and temperature for three different densities: 10^6, 10^7, and 10^8 cm^{-3}. As was anticipated in § II*c*, the ionization equilibrium is nearly independent of density. The temperature, on the other hand, is in the high-density limit determined by the γ-ray flux, $L_\gamma/4\pi r^2$, i.e., by $n\Gamma_\gamma$, whereas at low densities it only depends on Γ_γ. For $T_e \sim 5000$ K thermalization of the ^3P–^1D lines $\lambda\lambda$6300, 6364 sets in at $\sim 5\times 10^6$ cm^{-3}. In the interesting range $0.1 \leq x_e \leq 0.5$ we can approximate the effective ionization potential for O I by $\chi = 52(x_e/0.1)^{0.32}$ eV and can then obtain an approximate estimate of x_e as

$$x_e \approx 0.55\left[\left(\frac{M(^{56}\mathrm{Ni})}{0.1\ M_\odot}\right)\left(\frac{V_{\rm core}}{5000\ \mathrm{km\ s^{-1}}}\right)\left(\frac{t}{100\ \mathrm{days}}\right)\times\left(\frac{M}{1\ M_\odot}\right)^{-1}\right]^{0.43}\left(\frac{R}{r}\right)^{0.86}e^{-t/264\ \mathrm{days}}\,. \qquad (9)$$

This can also be expressed in terms of Γ_γ as

$$x_e \approx 0.16\Gamma_\gamma^{0.43}\,, \qquad (10)$$

These approximations are valid for $x_e \leq 0.5$ and fit the numerical calculations well in this range. From equation (9) we see that the degree of ionization will in general be higher than 0.1, increasing toward the center of the remnant. The degree of ionization is also expected to decrease relatively slowly with time as long as t is less than $\sim$300 days. These models only include cooling by [O I]. As we will see later, this is under many conditions a reasonable approximation. Even though the density is 10^8–10^9 cm^{-3}, there are very few channels other than the forbidden lines, when the gas is neutral or at most singly ionized. The [O I] lines may thus be present far above the thermalization density.

The most interesting feature is the rapid fall in temperature below $T_e \approx 2500$–3000 K. Depending on the density, this occurs for $\Gamma_\gamma = 0.1$–1, and results in a drop to $\sim$300–1000 K. This drop in temperature is caused by the transition from cooling by forbidden transitions between two multiplets, to

© American Astronomical Society • Provided by the NASA Astrophysics Data System

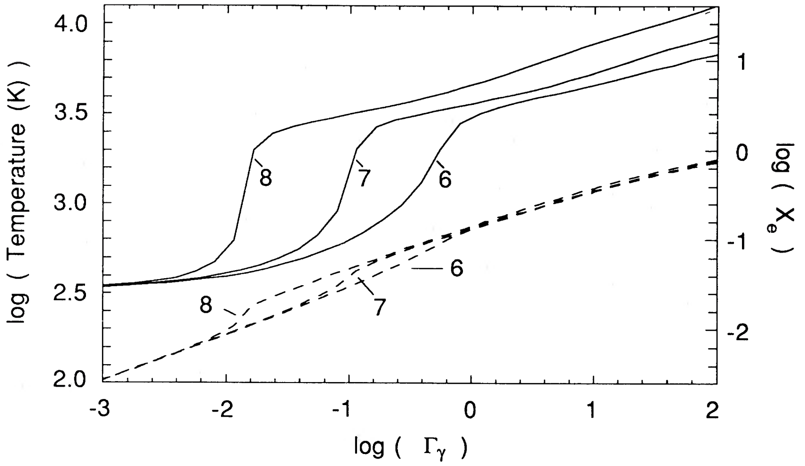

FIG. 5.—Temperature (*solid lines*) and electron fraction, $x_e = n_e/n_{\rm ion}$ (*dashed lines*), as a function of the γ-ray ionization parameter, Γ_γ. The temperature curves are labeled with the logarithm of the total oxygen density. The sharp drop in temperature is caused by the change from optical cooling to far-IR fine-structure cooling.

fine-structure cooling by infrared lines, most notably [O I] λλ63 and 140 μm. The cooling in these lines is nearly independent of the temperature, as long as the electron temperature is larger than the excitation temperature $T_{\rm ex} \sim 300$ K. Consequently, as the temperature falls below ~3000 K, when IR cooling takes over, the cooling will dominate the heating until $T_e \approx T_{\rm ex}$, when the Boltzmann factor becomes important for the fine-structure lines, and a balance can be established. This instability is similar to the "IR catastrophe" found for an iron plasma by Axelrod (1980*b*).

Since collisional de-excitation of the various forbidden lines is important, the ratios of these lines are an important diagnostic of the electron density and temperature, as is well known from the theory of planetary nebulae. The densities encountered here are usually higher, 10^6–10^8 cm^{-3}, and the populations close to LTE. For the specific case of SN 1985F this has recently been discussed by Begelman and Sarazin (1986). The most useful line ratios turn out to be [O I] λ5577/λλ6300, 6364, O I λ7774/[O II] and [C I] λ8727/λλ9824, 9850. An important assumption in this kind of analysis is that the lines must arise in the same region. The ionization structure is, however, sensitive to the distance from the center, as well as to a nonuniform density structure (eq. [9]). A "one-zone" analysis can therefore be misleading, especially when comparing the results of different ions, such as O I and O II, which are likely to arise in separate regions with large temperature and density differences. We will return to this type of analysis in the discussion of the observations of SN 1985 F in § VI*a*.

An interesting feature of the γ-ray–dominated model is that different lines directly reflect the various channels of the nonthermal electron losses. The energy going into the free electrons will heat them. This heating will then be balanced by various cooling processes, of which the most important is collisional excitation of low levels of the different ions present in the gas. With the exception of lines of Mg II, Ca II, and Na I, most of these are forbidden (e.g., [O I] λλ6300, 6364, 5577, [C I] λλ8727, 9824, 9850, [S II] λλ4071, 10320, [Ca II] λλ7291, 7324) or semiforbidden (e.g., Mg I] λ4571) transitions. Therefore, there will be a direct correspondence of the energy going into the electrons and that emitted in collisionally excited lines. In the same way, the energy going into ionizations will be balanced by radiative recombination losses. These are mainly permitted high-excitation transitions (e.g., O I λλ1302, 1356, 7774, 8446), and can have high excitation energies, difficult to excite below 10^4 K. These lines are therefore a measure of the ionization energy input from the nonthermal electrons. This type of argument was used in Fransson (1986) to estimate these contributions for SN 1985F.

IV. LINE PROFILES

The velocity field of the expanding supernova offers unique possibilities to obtain information about the physical conditions throughout the whole interior. At the epochs of interest the velocity of the gas has relaxed to a very simple form, $V(r) \propto r$. This result is basically kinematic, since any deviations from this homologous expansion will evolve into velocity discontinuities and thus cause dissipation, damping these perturbations. It is thus quite independent of the structure and initial conditions, and is confirmed by most calculations. The location of the points giving rise to emission at a certain frequency ν from a transition with rest frequency ν_0, is then given by

$$\frac{\nu - \nu_0}{\nu_0} = \frac{z}{r}\frac{v(r)}{c} = \frac{z}{R}\frac{V_0}{c}, \tag{11}$$

where z is the coordinate along the line of sight, R is the total radius of the envelope, and V_0 is the corresponding velocity. A given relative frequency shift, $\epsilon \equiv (c/V_0)[(\nu - \nu_0)/\nu_0]$ (≤ 1), thus corresponds to a disk $z/R = \epsilon$.

Now, consider a forbidden line where scattering can be neglected. The line profile is then given by

$$I(\epsilon) = 2\pi \int_{\epsilon R}^{R} j(r)n(r)^2 r\,dr , \tag{12}$$

where $j(r)$ is the emissivity defined so that $j(r)n(r)^2$ is the emission per unit volume. Since this quantity depends on the temperature and ionization structure, it is obvious that the line profile will reflect the structure of the supernova. We thus expect ions with high ionization potential to be concentrated to the center, and thus show narrower lines than, e.g., neutral ions. In the same way we expect the eventual onion structure of the synthesized elements to be reflected in the widths.

It is, however, probably more interesting to reverse the procedure, and apply this equation to the observations of the lines, and thus deduce the energy loss per unit volume as a function of radius from the profile. For this we differentiate equation (12) and obtain

$$j(r)n(r)^2\bigg|_{r=\epsilon R} = \frac{1}{2\pi\epsilon R^2}\,\frac{dI(\epsilon)}{d\epsilon}\,. \qquad (13)$$

Thus, we can directly obtain the emitted energy in the various transitions as a function of the radius in the remnant. If we then add the contributions from the different lines, we obtain the total energy loss. Since this must be balanced by the energy input from the γ-rays, the line profiles also map this quantity. In the simple, but important, case of one line dominating the total energy loss (e.g., [O I] $\lambda\lambda$6300, 6364) and an optically thin ($\tau_\gamma < 1$), central point source of γ-rays, we obtain

$$\frac{L_\gamma \kappa_\gamma \rho}{4\pi r^2}\bigg|_{r=\epsilon R} = \frac{1}{2\pi}\,\frac{dI(\epsilon)}{d\epsilon} \qquad (14)$$

or

$$\rho(\epsilon R) \propto \epsilon\,\frac{dI(\epsilon)}{d\epsilon}\,. \qquad (15)$$

Therefore, we can obtain the total density distribution of the supernova directly from the slope of the line profile.

The assumptions behind equation (15) are spherical symmetry, $V(r) \propto r$, that the γ-rays act like a central point source, and no continuous absorption or scattering which can distort the line profile. The last assumption may be violated, especially in the early stages, since electron scattering may be important. An estimate of the electron scattering optical depth for an oxygen plasma is given by

$$\tau_e = 0.64x_e\left(\frac{M}{1\ M_\odot}\right)\left(\frac{V_{\rm core}}{5000\ {\rm km\ s^{-1}}}\right)^{-2}\left(\frac{t}{100\ {\rm days}}\right)^{-2}\,. \qquad (16)$$

From equation (9) we find that $x_e \approx 0.1$–0.4, and an optical depth of 0.1–1 can be expected, depending on the mass and expansion velocity of the core. Since the electron scattering is coherent in the frame of the electron, the macroscopic velocity will shift the frequency by an amount

$$\frac{\Delta\nu}{\nu} = \frac{v}{c}\,(\cos\theta_1 - \cos\theta_2)\,, \qquad (17)$$

where θ_1 is the angle between the direction of the incoming photon and the gas velocity and θ_2 that of the scattered photon and the gas velocity. Therefore, the maximum shift will be $2v/c$ in one scattering, occurring for a scattering in the direction opposite to that of the gas velocity. If we ignore second-order scatterings (valid if $\tau_e \ll 1$), then the result will be a red extension of the line by a factor of $2v/c$.

To model this process quantitatively, we have performed Monte Carlo calculations, using the same program as for the γ-ray scattering in § II*a*. For illustration we have taken a shell with inner velocity one-tenth of the maximum with an emissivity $j \propto r^{-2}$. The electron density is constant, and in Figure 6 the results are shown for total optical depths, τ_e, of 0, 1, and 5. For $\tau_e = 1$, one sees that an extended wing is present on the red side, whereas the peak is depressed in order to conserve the number of photons. Since most photons originate in the center ($v \approx 0$), the width of the line extends approximately to $2v/c$, in agreement with the discussion above. For $\tau_e = 5$ the wing extends to several times the usual velocity broadening as a result of multiple scattering, and the whole line has been completely distorted. For optical depths less then unity, as we expect in the stages of interest here, the distortions are, however, small, and we can probably neglect this effect when analyzing the line profile. For early stages ($t \leq 100$ days) electron scattering may, however, be a dominant effect for the observed line shapes.

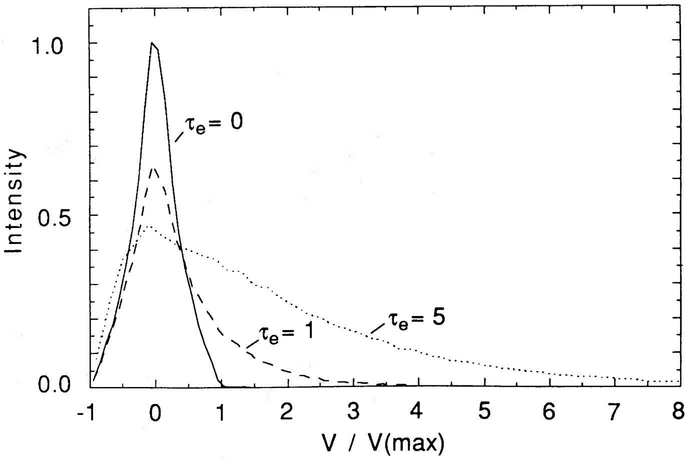

FIG. 6.—Effect of electron scattering on the line profiles for different optical depths τ_e. The emissivity has been taken as $j \propto r^{-2}$ outside of $r = 0.1R_{\rm max}$, and a constant electron density has been assumed.

V. MODEL RESULTS

In this section the model described in § II is used to study the general features of a supernova illuminated by γ-rays. As was discussed in § I, we expect two different scenarios where this situation is relevant, the low-mass exploding white dwarf and the high-mass collapsing core of a massive star. In this section we are mainly concerned with the late emission from massive core collapse supernovae. When discussing the origin of the Type Ib supernovae in § VI, we will also study some specific examples of exploding white dwarfs.

Nucleosynthetic models of massive stars of different masses have been calculated by Woosley and Weaver (1987). The familiar onion-type structure of these models reflects the different burning stages the star has undergone, with successively more heavy elements toward the center. It is thus of great interest to see how the energy input from the γ-rays is reflected in emission lines of these elements and, if possible, to use these for the determination of the elemental abundances. We will here study the general properties of these models, whereas in § VI we will discuss the application to observed supernovae. Since the density distribution and core velocity are important for the relative strengths, we start with a discussion of these.

The density of the core depends sensitively on the structure of the progenitor. In general, a point explosion in a uniform medium is expected to lead to a thin Sedov-like shell with an almost empty interior, although the ingoing rarefraction wave can widen the shell considerably (Chevalier 1976). The presence of steep density gradients, like that separating the envelope from the mantle, as well as radioactive heating, can change this situation considerably. In the simple case of two density components, a reverse shock propagating into the inner, dense region will form, if the mass of the outer, low-density component exceeds that of the core. This is probably the case for a standard Type II supernova which has undergone no mass loss (Weaver and Woosley 1980). In that case the

H envelope, with roughly two-thirds of the total mass, is massive enough to brake the expansion of the core. The result is a central high-density region, with a fairly uniform density. Models for SN 1987A, with a ZAMS mass of 20 $M_\odot$ and with a 5–14 $M_\odot$ H envelope at the time of the explosion, give O core velocities of ~ 1000 km s^{-1} (Woosley 1988; Nomoto, Shigeyama, and Hashimoto 1987). An interesting result of these models is that the heating of the central regions by the γ-rays during the first days results in a highly nonuniform density structure, with a central region of low density and most of the O core mass in a very thin shell. The peak coincides with the outer intermediate-element region and the inner parts of the oxygen shell. Outside the peak, the density decreases rapidly, until the He layer is reached, where the density gradient flattens.

Stars more massive than ~ 20 $M_\odot$ may lose all or a large fraction of the envelope due to mass loss before the explosion, making the progenitor a Wolf-Rayet–type star. WW have calculated hydrodynamic explosions of several massive He cores without H envelopes, and in Ensman and Woosley (1988) the resulting light curves are discussed. Because of the unhindered expansion, the core velocities are much higher. An 8 $M_\odot$ He core (ZAMS mass 25 $M_\odot$) with a total energy of 9.8×10^{50} ergs gave a velocity of 2614 km s^{-1} (WW model 8B). A higher core velocity would result if part of the He mantle was also lost, or if the explosion energy was higher. In the same way as for the progenitors with a H envelope, a central low-density region due to the ^{56}Ni heating is present, with most of the core mass in a thin shell.

The precise structure of the high-density oxygen region is rather uncertain, since it is likely that this region is subject to the Rayleigh-Taylor instability. This may smooth the density peak considerably, as well as produce elemental mixing. There are observational indications that this happens (§ VI*b*).

To see how the observed spectrum reflects the density and abundance structure of the supernova, we will keep the value of the He core mass constant, equal to 8 $M_\odot$ (ZAMS mass 25 $M_\odot$). The result of varying this is discussed in § V*c*. As input models we take the WW models 8A and 8B, with total kinetic energies, including the helium shell, of 9.8×10^{50} and 2.9×10^{51} ergs, respectively. The velocity at the outer boundary of the oxygen zone at 3.6 $M_\odot$ for model 8A is 2614 km s^{-1}, and for model 8B, 5100 km s^{-1}. The structure of model 8B at 200 and 300 days is given as models 1a and 1b, respectively, and for model 8A at 300 days as model 2. Because of the homologeous expansion in the coasting phase, we have rescaled the WW calculations according to $r \propto t$ and $\rho \propto t^{-3}$. Since observations of the Type Ib supernovae indicate that the velocity of the oxygen layer may be ~ 5000 km s^{-1}, we have taken model 8B as our "standard" model. To test the sensitivity of our results to the density distribution, we have also done one calculation with a uniform density, but otherwise the same structure as model 8B (model 3).

The total ^{56}Ni masses found by WW were 0.28 and 0.33 $M_\odot$ for the 8A and 8B models. For simplicity we have used 0.3 $M_\odot$ in both cases. Of the 8.43 $M_\odot$ He core, 2.45 $M_\odot$ resides in a compact remnant, which we ignore for the rest of the calculation. The remaining 5.98 $M_\odot$ has an outer He shell with a mass of 2.36 $M_\odot$, and an oxygen-dominated core region, with a mass of ~ 3.6 $M_\odot$. The abundances of the most important elements can be found in WW.

Together with the 15 $M_\odot$ model and a white dwarf model to be discussed in § VI, we give in Table 1 the main physical parameters, and in Table 2 the resulting line emission for the different models.

a) Temperature and Ionization

The general temperature and ionization structure of models 1–3 are all similar to that of model 1b (=model 8B) shown in Figure 7 at 300 days. The temperatures and degree of ionization given in this section refer to this model. In the figure the dotted line gives the expansion velocity from WW. Both the electron fraction and the temperature curves show that the supernova can be divided into three distinct regions, corresponding to the iron-cobalt core, the intermediate oxygen region, and the outer helium-dominated mantle. In the Fe core, close to the γ-ray source, the density is low because of the previous ^{56}Ni heating, and the ionization parameter is therefore high, resulting in a relatively high level of ionization

TABLE 1

MAIN PARAMETERS OF THE MODELS

Parameter	Model							
	1a	1b	2	3	4	5	6a	6b
ZAMS mass	25	25	25	25	15	15	1.4	1.4
He core mass	5.83	5.83	5.82	5.83	2.68	2.68	...	...
O core mass	3.66	3.66	3.66	3.66	1.02	1.02	...	...
$M(^{56}\mathrm{Ni})$	0.3	0.3	0.3	0.3	0.1	0.1	0.2	0.2
V_{core}(km s^{-1})	5140	5140	2680	5116	2409	1200	5390	5390
Density model	WW 8B	WW 8B	WW 8A	Constant	WW 4A	WW 4A	W86	W86
Time (days)	200	300	300	300	300	300	200	300
L_γ(10^{41} ergs s^{-1})	7.06	2.94	2.94	2.94	0.98	0.98	4.71	1.96
τ_γ(total)	0.45	0.20	0.81	0.26	0.36	1.45	0.24	0.10
$\Delta\tau_\gamma$(Fe)	0.090	0.040	0.14	0.067	0.040	0.16	0.13	0.06
$\Delta\tau_\gamma$(Si-Ca)	0.065	0.029	0.11	0.041	0.025	0.10	...	...
$\Delta\tau_\gamma$(O-Mg)	0.16	0.072	0.35	0.081	0.20	0.81	0.10	0.04
$\Delta\tau_\gamma$(O-C)	0.073	0.033	0.14	0.030	0.030	0.12	...	...
$\Delta\tau_\gamma$(He)	0.060	0.027	0.072	0.025	0.063	0.25	...	...
τ_e	0.16	0.06	0.16	0.09	0.07	0.19	0.09	0.03

NOTE.—All masses are in solar masses. The He core and O core masses do not include the neutron star. The γ-ray optical depths, $\Delta\tau_\gamma$, of the different abundance regions are well defined only for models 8A and 8B. For model 4A the O-Mg zone in reality contains $\sim \frac{1}{3}$ in Si-Ca elements, and for the deflagration model we lump all non-Fe zones together. The density structure is from WW and from Woosley 1986 (W86).

TABLE 2

LUMINOSITIES OF THE MOST IMPORTANT LINES FOR MODELS IN TABLE 1

		Model							
Species	λ[b]	1a	1b	2	3	4	5	6a	6b
He I	5876	0.24	0.05	0.12	0.06	0.04	0.08	0.07	0.02
	4471	0.08	0.02	0.03	0.02	0.01	0.02	0.01	0.01
	7065	0.12	0.02	0.07	0.03	0.02	0.06	0.06	0.01
	10830	1.51	0.33	0.68	0.36	0.06	0.57	0.37	0.07
C I	2967	4.68	0.45	1.79	0.43	0.39	1.21	5.87	0.26
	8727	8.05	1.60	4.32	1.58	1.30	2.13	11.71	1.80
	9824, 9850	0.70	0.53	0.59	0.52	0.22	0.22	1.02	0.60
C II	2324–2328	2.53	0.19	0.44	0.17	0.09	0.20	2.05	0.06
O I	5577	2.81	0.11	2.36	0.10	0.05	1.22	0.40	0.01
	6300, 6364	33.92	11.78	20.59	12.28	1.20	3.22	6.15	1.91
	1302	1.94	0.64	0.82	0.65	0.14	0.14	0.33	0.09
	1356	5.00	1.16	2.56	1.11	0.32	0.45	0.70	0.16
	7774	1.11	0.20	1.96	0.19	0.10	0.66	0.15	0.03
	8446	0.38	0.10	0.51	0.10	0.03	0.26	0.06	0.01
	63.15 μm	0.13	0.14	0.16	0.14	0.02	0.03	0.03	0.03
O II	2470	0.86	0.06	0.18	0.08	0.01	0.01	0.19	0.01
	3726, 3729	0.07	0.02	0.02	0.02	0.00	0.00	0.02	0.01
	7320, 7331	1.12	0.07	0.24	0.10	0.01	0.02	0.25	0.02
O III	4959, 5007	0.19	0.04	0.03	0.06	0.01	0.00	0.08	0.02
Ne II	12.81 μm	0.33	0.30	0.26	0.34	0.06	0.03	0.01	0.00
Na I	5890, 5896	3.18	0.53	11.45	0.13	0.66	3.48	1.38	0.22
Mg I	4571	5.83	0.82	11.27	0.38	0.35	2.88	0.70	0.07
Mg II	2796, 2803	30.63	3.47	4.09	4.84	0.60	1.82	0.14	0.01
Si I	1.099 μm	3.47	0.49	3.52	0.56	1.33	2.81	0.29	0.06
	1.636 μm	1.14	0.74	1.22	0.61	0.71	0.95	0.10	0.07
Si II	2328–2350	1.21	0.04	0.26	0.06	0.02	0.51	0.01	0.00
S II	4069, 4076	0.84	0.11	0.51	0.23	0.17	1.83	0.06	0.01
	10287–10371	0.55	0.07	0.39	0.15	0.12	0.97	0.04	0.01
Ar II	6.985 μm	0.24	0.27	0.06	0.16	0.25	0.07	0.03	0.03
Ca II	3950	1.44	0.02	1.53	0.03	0.32	2.05	0.10	0.00
	7291, 7324	24.22	6.80	5.89	9.31	7.02	5.25	3.01	1.06
	8498–8662	5.79	0.15	3.53	0.33	2.17	3.97	0.53	0.03
"Fe I"	...	14.36	2.99	17.13	6.20	1.53	9.84	12.20	2.81
"Fe II"	...	41.67	6.57	21.70	14.37	1.74	6.72	39.13	6.69
Total	...	232.66	51.52	142.24	66.69	22.43	58.71	93.05	17.90

[a] In units of 10^{39} ergs s^{-1}.

[b] Wavelengths in angstroms unless noted.

$[\Gamma_\gamma \propto 1/(nr^2)]$. Owing to the efficient Co-Fe cooling, the temperature is only $\sim$3500 K. In the thin S-Si layer the density rises and the cooling efficiency decreases somewhat. Therefore, the number of free electrons falls abruptly, and the temperature increases to $\sim$4100 K, with most of the cooling due to Ca II. In the oxygen region the temperature is in the range 4500–5000 K, and the electron fraction is $x_e \sim 0.2$–0.3. A slight increase in temperature takes place in the outer parts, where carbon becomes abundant at the expense of magnesium. At the oxygen-helium boundary a dramatic increase in temperature to $\sim$8000 K and a decrease in x_e to $\sim$0.15 takes place. This is due to the inefficient cooling of He I, which has no low-excitation levels easy to excite thermally. Instead, most of the cooling is due to C I, O I, Mg II, and Ca II. The drop in x_e is due mainly to the high value of the effective ionization potential of He I ($\sim$46 eV at $x_e = 10^{-4}$, increasing to $\sim$100 eV at $x_e = 0.2$). Model 1a at 200 days has an ionization structure similar to that of model 1b, which is expected from equation (9). Because of the higher γ-ray flux the temperature in the oxygen region is slightly higher, $\sim$5800–6500 K, as well as the temperatures in the Fe core and the He shell.

While the ionization equilibrium of the dominant elements in the different zones is set mainly by the γ-ray ionization, the trace elements with low ionization potentials, such as Mg I, Na I, and Si I, are dominated by photoionization due to diffuse radiation below $\sim$11 eV. This is produced mainly by recombination and collisionally excited lines of the abundant elements, like the O I lines at 1302 and 1356 Å, C II] λ2326, and Si II] λ2335. The intensities of these lines are sensitive to absorption and scattering by both continuous bound-free absorption and scattering by the many UV resonance lines. The effect of the resonance scattering in the envelope by lines from singly and doubly ionized elements is especially striking in the UV spectrum of SN 1987A (e.g., Fransson *et al.* 1987; Lucy 1987). While the velocities in the core are considerably lower, making the blanketing from each line less efficient, the abundances are high and blanketing could be quite important. Since this redshifts the photons, the intensity of ionizing photons will decrease and the ionization of these elements will be lower. We have not modeled this process in any detail, but, with a complete neglect of the emission in the O I lines mentioned, the Na I, Mg I, and Si I abundances changed by large factors (i.e., more than factors of 2). A similar effect occurs as a result of bound-free absorption by these elements. This is especially sen-

1989ApJ...343..323F

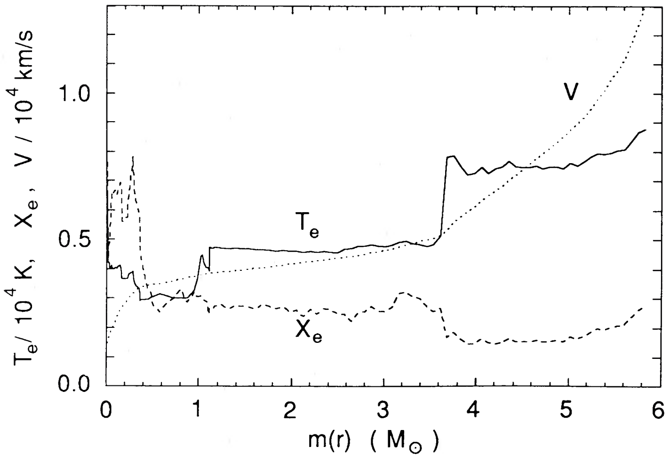

FIG. 7.—Temperature and electron fraction, model 1b (ZAMS mass 25 $M_\odot$, He core mass 8 $M_\odot$), 300 days after the explosion. The dotted line shows the velocity, taken from WW. The different burning zones are clearly seen in the temperature structure.

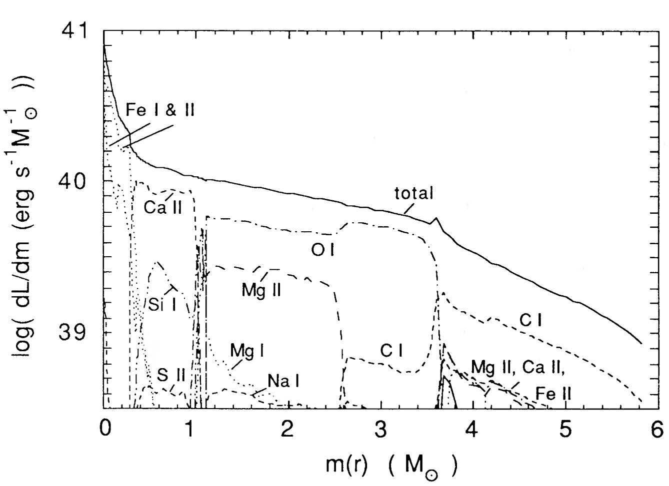

FIG. 8.—Luminosity per unit mass, dL/dm, of the most important lines for model 1b in Fig. 7.

sitive to the density, which can be seen in models 1–2, and in models 4–5, where the fraction of neutral elements rises by a large factor in the high-density peak. The strengths of lines from these elements are therefore very sensitive to both these effects. Charge transfer may also be important for both ionization and recombination. Unfortunately, rates for many reactions are lacking (see Appendix B), but the importance of this process can be seen in the ionization of Ca. Where Ca I and O II coexist, the ionization equilibrium is completely dominated by the reaction Ca I($^1S_0$) + O II($^4S^o$) → Ca II($5p\ ^2P_{1/2}$) + O I(^3P). The inverse reaction is not important, since it proceeds through the excited Ca II($5p\ ^2P_{1/2}$) state. This reaction is sufficient to keep Ca ionized in most of the core.

With the marginal exception of the low-velocity model 5, all models have γ-ray optical depths less than unity, implying a uniform energy deposition throughout the supernova. The optical depth to electron scattering for optical photons is between 0.03 and 0.16 for all models (Table 1).

b) *Line Emission*

Whereas the overall temperature and ionization structure do not vary much between the models, the fluxes in the emission lines can differ by large factors in some cases. Since the different lines also have their origin in different abundance zones, and thus different velocity ranges, the observed line strengths and profiles can give important information about the supernova structure.

By a simple consideration of the energetics of the various shells, we can understand many of the features of the spectra. The total energy per unit time absorbed by the envelope is $\sim(1 - e^{-\tau_\gamma})L_\gamma$, and the luminosity from a shell of mass Δm at radius r is $\Delta\tau_\gamma L_\gamma \sim \Delta m \kappa_\gamma L_\gamma/4\pi r^2$. In Table 1 the γ-ray optical depths of the different abundance shells are given, which should be compared with the total luminosities from the elements in the shell. Considering model 1b, 23% of the emission comes from lines of Co-Fe, 22% from Si-Ca, 13% from Na-Mg, 35% from O, and 9% from C. As we will discuss below, Mg and O dominate the emission of the O-Mg and O-C zones, whereas C dominates the emission from the He shell. Taking this into account, we find good agreement with the relative values of $\Delta\tau_\gamma$ for the respective zones. Thus, *the fluxes from the different burning shells are sensitive not only to the mass of the elements but also to the hydrodynamic structure of the envelope*, which can be directly seen when comparing models 1, 2, and 3, which differ only in this respect. The use of the line profiles to locate the position of the shell is therefore extremely important for the abundance determination.

The ratio of recombination emission to collisionally excited line emission is directly related to the deposition of the nonthermal electron energy in the gas (§ III*c*). The recombination lines are calculated explicitly only for O I and He I. Comparing the total emission from the O-shell (including O I, Na I, Mg I, Mg II) with that in the recombination lines, we find a ratio of ~0.10–0.12 for models 1–3. The electron fraction is ~0.3 in the O shell, and Figure 3 shows that for this value of x_e the ratio of the energy going into ionizations to that of heating is 11:4.5. There is thus a rough agreement with the total emission expected. The fraction of this coming out in, e.g., the 7774 and 8446 Å lines depends on optical depth effects in the lines, and varies considerably between the models (Table 2).

When discussing the individual lines from the various zones, it is instructive to plot the luminosity per unit mass for the various lines as a function of the mass (or radius) from the center. This directly gives the contribution of a given abundance zone to the line strengths, displayed in Figure 8 for model 1b. Starting with the innermost region, 0–0.30 $M_\odot$ (measured from the mass cut), this is completely dominated by Fe and Co emission. Although not calculated here, one can see from Axelrod (1980*b*) that since the temperature is 3500–4000 K in this region, most of the emission will emerge in the visible region as lines of Fe II. A slightly lower temperature (~3000 K) would transform most of the emission into the IR.

The next region, 0.30–0.81 $M_\odot$, is characterized by the Si group elements. This is also the outermost region whose composition is substantially modified by the passage of the shock wave. ^{28}Si and ^{32}S are most abundant, with ^{36}Ar and ^{40}Ca lower by a factor of ~10. We find that for most of the models [Ca II] $\lambda\lambda$7291, 7324, the IR triplet, and [Si I] $\lambda\lambda$1.099 and 1.636 μm dominate the emission. A small fraction also emerges as [S II] $\lambda\lambda$4069, 4076, 10287–10370, [Si II] λ34.82 μm, and [Ar II] λ6.985 μm. The latter lines are useful for determining the abundances of these elements.

The relative strengths of the Ca II H and K lines, the IR triplet, and the forbidden 7291, 7324 Å lines depend rather sensitively on the density and temperature of the region. In

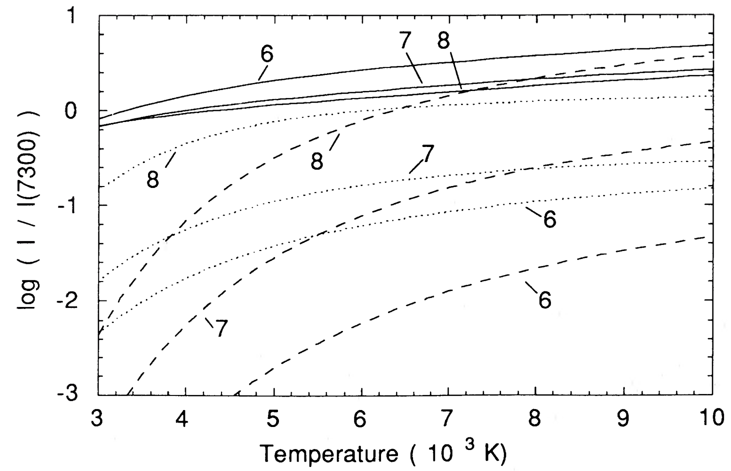

FIG. 9.—Strengths of [O I] λλ6300–6364 (*solid lines*), Ca II λλ8498–8662 (*dotted lines*), and the Ca II H and K lines (*dashed lines*), relative to [Ca II] λλ7291–7324 ("7300"). The relative abundance of Ca II to O I is here 10^{-3}, by number, but the [O I]/[Ca II] flux scales with this quantity. The lines are labeled by the logarithm of the electron density.

Figure 9 the ratios of the IR triplet and the H and K lines to the 7291, 7324 Å lines are shown as a function of temperature, and for electron densities of 10^6–10^8 cm^{-3}. For this calculation photoionizations from the excited states are neglected, so that the only variables are the density, the temperature, the number of Ca II ions, and the time. The last two parameters only enter the optical depths of the lines, and we can use optical depth as a parameter. The optical depth in the H and K lines is $\sim 5.5 \times 10^6[X(\text{Ca II})/10^{-3}](n/10^8\ \text{cm}^{-3})t_{\text{yr}}$, and for the forbidden 7300 Å lines it is, a factor of $\sim 1.7 \times 10^6$ lower. Here X(Ca II) is the ratio of the number density of Ca II ions to the total number density. A variation of the Ca II abundance between 10^{-4} and 10^{-2} influences the results only weakly. Above $\sim 10^7$ cm^{-3} both the H and K lines and the IR triplet are close to LTE, and their strengths are a function of the temperature only. Below this density the ^2P level is severely underpopulated, and below ~4500 K the population of the ^2P level is low even in LTE, and both the H and K lines and the IR multiplets are therefore weak. The smaller optical depth of the 7291, 7324 Å lines causes thermalization to occur at a considerably higher density than for the others. Therefore, a low temperature and density favor the 7291, 7324 Å lines. Except for the high-density model 6, the H and K lines are also very weak.

The oxygen zone can be divided into two distinct regions, one between 0.81 and 2.55 $M_\odot$, where most of the ^{12}C has been transformed into ^{20}Ne, ^{24}Mg, and ^{28}Si by α-captures, and one ^{12}C-rich between 2.55 and 3.64 $M_\odot$, where the composition is just the result of the 3α process. Even though oxygen dominates the abundance of magnesium by a factor of ~15 in the inner of these regions, the strong Mg II resonance line at 2800 Å has a strength comparable to or even larger than [O I] λλ6300, 6364. In the high-density peak most of the magnesium is found in the form of Mg I, and consequently collisional excitation of Mg I] λ4571 dominates the cooling, This explains the strength of this line in the models with the highest density, models 1a, 2, and 5. Other less important coolants are [O I] λ5577 and [Ca II] λ7300. In the outer oxygen zone ^{24}Mg drops by a factor ~30, and ^{12}C instead becomes abundant. There is thus no competition with any permitted or semiforbidden lines, and [O I] λλ6300, 6364 is the strongest line, together with [C I] λ8727. At epochs less than ~450 days the density in the core can be so high that forbidden lines, like [O I] λλ6300, 6364 and [Si I] λ1.0991 μm, are optically thick. This results in a decrease in their cooling efficiency and may give a P Cygni type of absorption component in the blue wings of these lines.

Finally, in the He shell (if present), we have the familiar situation that the most abundant element is difficult to detect. The strongest line in all models is the ^3P–^3S 10830 Å transition. This is because the 2 ^3S level is metastable, with a large population. Collisional excitation from this level is thus important, as well as conversion from other transitions to this level because of the high optical depth. The 5876 Å line is less affected by these effects, and most of the emission is due to recombination. Most of the cooling in this zone is controlled by [C I] λ8727, C I λ2966, C II] λ2326, Mg II λ2800, and [Ca II] λ7300, in this order. The low flux of [O I] λλ6300, 6364 is a result of the small oxygen abundance in this zone, C/O ~ 6. For model 1b most of the [C I] λ8727 emission is produced here. The presence of the He zone may be observed as an extended, weak high-velocity wing of these lines (see § VI*b*).

An important question for the determination of abundances of the supernovae is how the density structure of the envelope affects the observed line strengths. As discussed in § IV, and as will be demonstrated in § VI, it is possible to infer this directly from the line profile. By comparing the results of the highly nonuniform model 1b with the uniform-density model 3 and the low-velocity model 2, we can get an idea of which lines are most sensitive to this. The velocity of the outer boundary of the oxygen zone in model 3 has been set to roughly the same value as for model 1b. Comparing these models, one sees that the major change is in the optical depth of the Fe region, which is reflected in a considerably higher value of the Fe I and Fe II emission. Also, the Mg I] λ4571/Mg II λ2800 ratio differs from model 1. This effect is discussed below.

In the low-velocity model 2 (=model 8A), the density is a factor of ~8 higher than in model 1b. The structure is otherwise similar. A similar variation, of course, also results by comparing the same model at different epochs, since $\rho \propto (Vt)^{-3}$ (cf. model 1a). While the total emission from the different zones is determined by their column densities, the line ratios within a given zone may vary considerably. In the Si-Ca zone nearly all of the emission is due to [Ca II] λ7300 in model 1a, while in model 2 [Si I] λλ1.099, 1.645 μm have nearly the same

© American Astronomical Society • Provided by the NASA Astrophysics Data System

strengths. The higher density also makes the Ca II IR triplet and the H and K lines stronger at the expense of the 7300 Å lines, in agreement with Figure 9. As expected, the [O I] $\lambda\lambda6300$, 6364/$\lambda5577$ ratio decreases by a factor of ~10 from model 1b to model 2. In contrast to model 1b, the Mg I] $\lambda4571$ and Na I D lines dominate the Mg II resonance line. The high density in these models decreases the effect of photoionization by the diffuse radiation, resulting in fairly high abundances of those ions and large line strengths. Therefore, the most model-dependent lines are the Na I, Mg I] and [Si I] lines, while the others are more reliable since they are not affected appreciably by photoionization.

c) Line Ratios as a Diagnostic of the Core Mass

The relative abundances of the different elements vary substantially with the mass of the He core. It is thus of interest to see how this is reflected in the line ratios of the different ions. For this reason we have run two models with a He core mass of 4 $M_\odot$, WW model 4A (ZAMS mass 15 $M_\odot$), given as models 4 and 5 at 300 days in Tables 1 and 2. These differ in that model 4 has an O core velocity of 2500 km s^{-1}, whereas model 5 is scaled to an expansion velocity of ~1200 km s^{-1}. The high-velocity model is characteristic of a bare He core, and the low-velocity model is that expected for a Type II supernova with a H envelope.

A major difference between models 8A and 4A in terms of the abundance structure is that the inner part of the O shell (between 0.14 and 0.81 $M_\odot$) in the 4A model has a large fraction ($\sim40\%$) of Si-Ca mixed with the O and Mg. Although small, the Ca mixing is crucial (Ca/O $\sim 6 \times 10^{-2}$, by number), since Ca II is a factor of $\sim10^2$–10^3 more efficient in cooling than O I (Fig. 9). Consequently, most of the emission from this zone emerges not as [O I] but as [Ca II] $\lambda\lambda7291$, 7324, with [Ca II] $\lambda\lambda7291$, 7324/[O I] $\lambda\lambda6300$, 6364 $\sim$ 5.6 for model 4. Therefore, the difference between the spectra of the 4 and 8 $M_\odot$ He core is mainly due to the different degrees of mixing, although the different total Ca/O ratios, 0.011 in model 8A and 0.106 in model 4A, contribute to the increase. Further examples of this effect are given in § VI*b*. In the outer part of the O shell, C is much more abundant than in model 8A, and [C I] $\lambda8727$/[O I] $\lambda\lambda6300$, 6364 $\sim$ 1.05, 6 times as high as in model 1b.

Model 5 with a O core velocity of only 1200 km s^{-1} shows the same effects of the ~8 times higher density compared with model 4, as we have already discussed for models 1b and 2: The Na D and Mg I] lines are strong, as well as [O I] $\lambda5577$ and the H and K lines. The variation of the [O I] $\lambda\lambda6300$, 6364/5577 ratio and those of Ca II with density make these lines valuable as rough diagnostics of the local conditions. The [Ca II] $\lambda\lambda7291$, 7324/[O I] $\lambda\lambda6300$, 6364 ratio has decreased to only ~1.6, because of the higher density.

From this discussion we conclude that *mixing makes it difficult to derive relative abundances solely from the line strengths.* These are a result of *both* the relative abundances and their distributions. However, *by combining the line strengths with the information from the line profiles, it is possible to disentangle these effects.* In model 1b the [Ca II] profile extends to only $\sim60\%$ of the velocity of the [O I] line; the two have very similar extensions for model 4. In both cases the profiles are flat, which results from the shell structure of the density distributions. Since the degree of mixing is sensitive to the treatment of the convection in the supernova progenitor and during the explosion, this illustrates that the late observations may help in understanding these processes.

d) Time Dependence

The time dependence of the emission-line luminosities depends on the decaying γ-ray input, proportional to $\tau_\gamma L_\gamma \propto t^{-2}e^{-t/114\ \mathrm{days}}$, and the decreasing density, $\rho \propto t^{-3}$. By comparing model 1a at 200 days and model 1b at 300 days in Table 2, where the total energy input has decreased by a factor of 5.4, we can see how the more subtle effects of the density decrease affect the results. We first note that the γ-ray ionization parameter, $\Gamma_\gamma \propto te^{-t/114\ \mathrm{days}}$, decreases by a factor of 1.6, and thus the degree of ionization decreases by a factor of 1.3 ($x_e \propto \Gamma_\gamma^{1/2}$, eq. [10]). Therefore, the electron fraction is not changed appreciably, and the electron density follows the total density decrease. The main effect of this is that collisional excitation and de-excitation become less effective with time, which favors the populations of the low-energy levels. The effect of this can be seen in the [C I] $\lambda8727/\lambda\lambda9824$, 9850, [O I] $\lambda5577/\lambda\lambda6300$, 6364, and [Si I] $\lambda1.099$ μm ratios, which all decrease by factors of 4–8 from model 1a to model 1b. A similar effect for Ca II is apparent, where the forbidden 7291, 7324 Å lines completely dominate the Ca II emission in model 1b at the expense of the H and K lines and the IR triplet (cf. Fig. 9). The fine-structure lines are not affected by the density decrease, since they are in LTE and the emission then depends only on the total mass of the ion, which does not change much. This explains the constant luminosity of the [O I] $\lambda63.15$ μm, [Ne II] $\lambda12.81$ μm, and [Ar II] $\lambda6.985$ μm lines, and makes them less model-dependent and thus suitable for abundance determinations. Although the total ionization does not vary much, some of the low-ionization ions dominated by photoionization can change appreciably. This is due to the sensitivity of the ionizing UV flux to the continuous absorption in this region of the spectrum (§ V*a*). The recombination lines follow the γ-ray input closely, although optical depth effects in, e.g., the O I 8446 and 7774 Å lines can complicate their behavior.

As discussed in § III, and in Fransson and Chevalier (1987), at late time the decreasing energy input may lead to a thermal instability. In the Type II models discussed in these papers this occurred at ~700 days. The models in this paper show the same general behavior, with a sudden temperature fall, as the cooling shifts from being dominated by optical and near-IR transitions to cooling by far-IR fine-structure lines. Most of the emission then emerges as far-IR lines, like [O I] $\lambda63.15$ μm, [Ne II] $\lambda12.81$ μm [Si I] $\lambda1.645$ μm, [Si I] $\lambda68.49$ μm, [S I] $\lambda25.25$ μm, and [Ar II] $\lambda6.985$ μm. In Figure 10 we show the temperature as a function of time in the oxygen shell at a fixed mass coordinate, 2.0 $M_\odot$, from the center. The thermal instability here results in a sudden drop of the temperature from ~2500 K to less than 700 K in ~200 days. This evolution shows the same general behavior as in the simple model in Figure 5, even though many other elements are included. In the case of a clumpy density distribution, the instability may set in earlier in the density peaks, and a two-phase situation may result. It is also possible that it may trigger the formation of molecules and dust in the metal-rich environment. Even before the instability sets in, below ~3500 K, molecule formation, in particular CO, may be important. Therefore it is interesting that recent observations of SN 1987A have shown evidence of CO in the ejecta (McGregor and Hyland 1987; Spyromilio *et al.* 1988).

VI. APPLICATION TO TYPE Ib SUPERNOVA SPECTRA

The main characteristics of the Type Ib supernovae are (1) association with H II regions, (2) radio emission, presumably due to circumstellar interaction, (3) underluminous compared

1989ApJ...343..323F

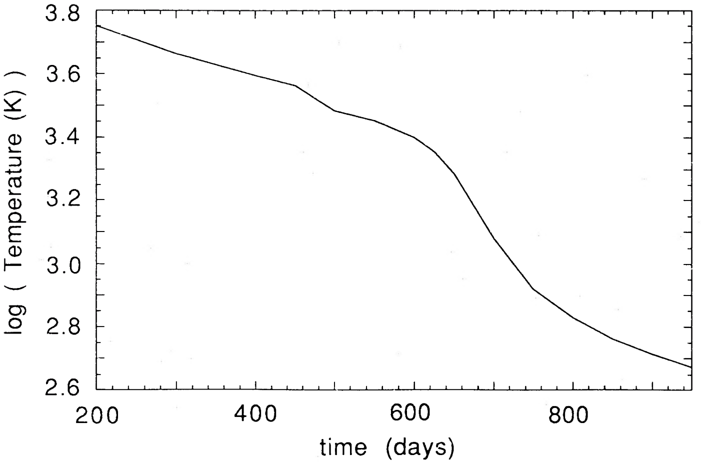

FIG. 10.—Temperature evolution at a fixed point [$m(r) = 2\ M_\odot$] in the oxygen shell for the WW model 8B. At ~650 days the thermal instability sets in.

to Type Ia's, indicating a smaller mass of ^{56}Ni, (4) after ~200 days the spectra are dominated by strong [O I] lines (see Panagia 1987 for review). As argued by several authors, most of these properties indicate a massive progenitor (Filippenko and Sargent 1985; Chevalier 1986; Fransson 1986; Wheeler and Levreault 1985; Schaeffer, Cassé, and Cahen 1987; Wheeler *et al.* 1987; Harkness *et al.* 1987). From a nebular analysis of the O I and O II lines, Begelman and Sarazin (1986) even proposed that SN 1985F was the result of the explosion of a ~50 $M_\odot$ Wolf-Rayet star, which had undergone a pair-instability collapse. Since the frequency of Type Ib's is comparable to that of the Type Ia's (Panagia 1987), this origin is unlikely to apply for all Type Ib's. Harkness *et al.* (1987) identify a number of strong He I lines in the early spectra in the Type Ib's SN 1983N and 1984L. This is expected in the massive star scenario, but not from an exploding C-O white dwarf. Light curves for exploding He cores have been calculated by Ensman and Woosley (1988). Compared with the observed Type Ib light curves, they seem to give too wide a peak for a core of more than ~4 $M_\odot$. However, since the density distributions of these models do not reproduce the observed line profiles (see § VI*b*), it is too early to make any definite conclusions. It has also been suggested that the Type Ib's could be the result of a white dwarf explosion, where the deflagration wave could have died out either very quickly (Woosley 1986) or as a result of a three-dimensional off-center point detonation (Branch and Nomoto 1986). In both cases most of the white dwarf's composition remains unaffected by the explosion. Iben *et al.* (1987) have shown how the binary evolution of a He white dwarf and a CO white dwarf might lead to an off-center detonation.

The late observations of SN 1983N (Gaskell *et al.* 1986), SN 1984L (Schlegel and Kirshner 1989), and SN 1985F (Gaskell *et al.* 1986; Filippenko and Sargent 1985, 1986, hereafter FS85, FS86) have given us a unique opportunity to study the interior of the supernova. These spectra were characterized by a limited number of strong emission lines superposed on a weak continuum. Because of this and the high quality of the spectra, reliable line identifications could be obtained, in contrast to ordinary Type Ia supernovae. Although SN 1985F was discovered long after maximum light, photographic prediscovery observations exist, showing that the first spectroscopic observations were made ~270 days after the explosion (Tsvetkov 1986). Compared with the Type Ia light curves, both the post-maximum decline and the decline later than ~100 days were considerably slower. Since both the diffusion time scale and the γ-ray trapping increase with the mass, this argues for a larger mass than for the Type Ia's. SN 1983N was discovered before maximum light (Panagia *et al.* 1988), and the nebular [O I]-dominated spectrum appeared ~250 days after maximum light. Comparison of these spectra with those of the standard Type Ia SN 1981B (Branch 1984) taken 270 days past maximum shows a striking difference, strongly indicating a different origin.

a) Observed Line Strengths of SN 1985F and Nebular Diagnostics

As the simplest approach, one may use the different forbidden lines to estimate the density and temperature in the envelope. The crucial question is whether these considerations can rule out the exploding white dwarf in favor of a massive star. This has already been discussed in an interesting paper by Begelman and Sarazin (1986, hereafter BS); here we study their arguments in more detail and also include some other useful density- and temperature-sensitive lines. It is also important to discuss the accuracy and limitations of this type of analysis, e.g., in connection with the late time observations of SN 1987A.

From the observations there are a number of interesting line ratios, which are sensitive to the temperature and density. BS used the [O I] $\lambda\lambda$6300, 6364/λ5577 and the O I λ7774/[O II] λ3728 ratios. In addition to these, the Ca II lines (Fig. 9), [C I] $\lambda\lambda$9824, 9850/λ8727, [S II] λ6728/λ4071, and [Si I] λ1.099 μm/λ1.646 μm ratios may provide additional constraints. The absolute luminosity of the [O I] $\lambda\lambda$6300, 6364 lines (or any other!) then gives an estimate of the mass of O I needed to emit this energy, at a particular temperature and electron density. In the case of a thermalized line, the mass will be proportional to the luminosity.

Since the difference in the mass by a factor of 2 implies a completely different progenitor, errors and uncertainties in the observed quantities are important to consider. We therefore start with a discussion of the probable range of the observed quantities for SN 1985F. Except for the observational errors, there are two main uncertainties in the analysis, the reddening and the distance to NGC 4618. The reddening affects both the luminosity and the relative line ratios, if the wavelengths of the lines are very different, e.g., in the O I λ7774/[O II] $\lambda\lambda$3726, 3729 ratio. FS85 estimate that $A_V \sim 1$ mag from the Hβ:Hγ ratio of a superposed H II region. As they point out, this value need not necessarily apply to the supernova, although this is a likely possibility, if the supernova progenitor was a massive star. Assuming a lower limit of $A_V = 0$ (since Galactic absorption is unimportant), this means that the [O I] $\lambda\lambda$6300, 6364 luminosity could be smaller by a factor of ~2.5. Also the distance is uncertain by a factor of 2, corresponding to $H_0 = 50$ or 100 km s^{-1} Mpc^{-1}, implying an additional factor of ~4 in the luminosity. Since BS use $A_V = 1$ and $H_0 = 50$, L([O I]) ~ 5×10^{40} ergs s^{-1} is close to the upper limit. Taking the above uncertainties into account, this range should be extended considerably, and a more conservative estimate would be $0.5 \times 10^{40} \leq L([\text{O I}]) \leq 5 \times 10^{40}$ ergs s^{-1}. Since most limits on n_e and T_e come from the line ratios with small separation, these are not equally sensitive to the reddening. An exception is O I λ7774/[O II] $\lambda\lambda$3726, 3729, and for this reason it may be preferable to use the O I λ7774/[O II] $\lambda\lambda$7320, 7331

© American Astronomical Society • Provided by the NASA Astrophysics Data System

1989ApJ...343..323F

ratio instead. In this case there are, however, problems with the blending with [Ca II] λλ7291, 7324.

In our calculations we have used $A_V = 1$ mag for the line ratios. This choice does not affect our conclusions. For the ratio of [O I] λλ6300, 6364/λ5577 we use a lower limit of 28, since there is a feature at 5542 Å which may be due to [O I] λ5577. [O II] λλ7320, 7331 may be present as a blend with [Ca II] λλ7291, 7324, and to be conservative we take O I λ7774/[O II] λλ7320, 7331 > 1:8. The peak wavelength given by FS86, 7296 Å, may favor the [Ca II] identification, so this limit may actually be higher. For O I λ7774/[O II] λλ3726, 3729 we use a lower limit of 1.0, which takes into account the reddening correction. [C I] λλ9824, 9850 is definitely present, and the auroral line [C I] λ8727 is likely to be part of the wide blend at ~8700 Å, so [C I] λλ9824, 9850/λ8727 > 0.2. In fact, the peak wavelength of this, 8734 Å, indicates that most of the flux is from the [C I] line, while the broad wing to the blue is probably due to Ca II λλ8498–8662 and O I λ8446. Finally, we identify the line at 4306 Å with the [S II] λλ4069, 4076 doublet, which is more likely than Si I λλ3905–4103 or Mn I λλ4031, 4034, suggested in FS86. The corresponding [S II] λλ6716, 6731 lines cannot be seen in the wing of the [O I] line, so we take [S II] λλ6716, 6731/λλ4069, 4076 < 0.5. Since we are mainly interested in whether the white dwarf scenario can be ruled out in favor of the massive core, we plot the L([O I] λλ6300, 6364) curves for $M(\mathrm{O}) = 1\ M_\odot$. From the discussion above we concluded that this luminosity was highly uncertain, so we show the curves corresponding to luminosities of (1, 2, and 4) × 10^{40} ergs s^{-1}. (Alternatively, if one believes in a luminosity of 4 × 10^{40} ergs s^{-1}, corresponding to $A_V = 1$ and $H_0 = 50$, these curves correspond to 4, 2 and 1 $M_\odot$ of oxygen, respectively.) In calculating this function for a given total oxygen mass, one has to know the ratio O I/O II. This can be obtained from the O I λ7774/[O I] λλ6300, 6364 ratio, *if* one assumes that the two ionization zones coincide. Although not explicitly stated in their paper, this is the procedure used by BS. For the atomic data we use the recent compilation by Mendoza (1983), with the exception of O I λ7774, where we use the effective recombination rate given in Julienne, Davis, and Oran (1974).

Figure 11 shows that the [S II] constraint excludes very low electron densities, $\leq 10^5$ cm^{-3}. The [C I] and [O I] constraints are similar in nature, although the [C I] ratio is somewhat more restrictive. Since the [C I] ratio may not only be a limit, but may be close to the actual value, the T_e-n_e track from this is of special interest. The reddening-sensitive O I λ7774/[O II] λ3727 ratio turns out to be more interesting below $10^{5.6}$ cm^{-3}, whereas above the O I λ7774/[O I] λλ7320, 7331 ratio gives a firmer limit.

The locus of the L([O I] λλ6300, 6364) = 4 × 10^{40} ergs s^{-1} curve coincides approximately, although not in detail, with the BS 1 $M_\odot$ curve. BS's other curves also differ somewhat from ours, but it is difficult to trace the difference, since they do not give any details of their atomic data. If we put all contraints together, we find that *if* L([O I] λλ6300, 6364) < 1.5 × 10^{40} ergs s^{-1}, these constraints can marginally be satisfied by 1 $M_\odot$ of oxygen. As we have already remarked, it is, however, not likely that the O I and O II (as well as the C I and S II) lines arise in the same regions, and thus under the same conditions. The models in § V*a* show that O II in general dominates in the center. The O I λ7774/[O II] ratios could thus be satisfied by a separate combination of T_e and n_e from that of the [O I] lines, and the only strong constraints are the [O I] λλ6300, 6364/λ5577 ratio and L([O I] λλ6300, 6364). Since the O I/O II ratio in this case cannot be determined observationally, the latter constraint only gives a lower bound on the O I mass. Assuming that *no* other source of ionization than collisional is important, this lower limit in the n_e-T_e plane is shown by the dotted line in Figure 11, for a total oxygen mass of 1 $M_\odot$ and L([O I] λλ6300, 6364) = 10^{40} ergs s^{-1}. The allowed region is in this case given by the shaded area. With this more relaxed situation, it is possible to have $M(\mathrm{O}) \leq 1\ M_\odot$, even if L([O I] λλ6300, 6364) is as high as ~4 × 10^{40} ergs s^{-1}.

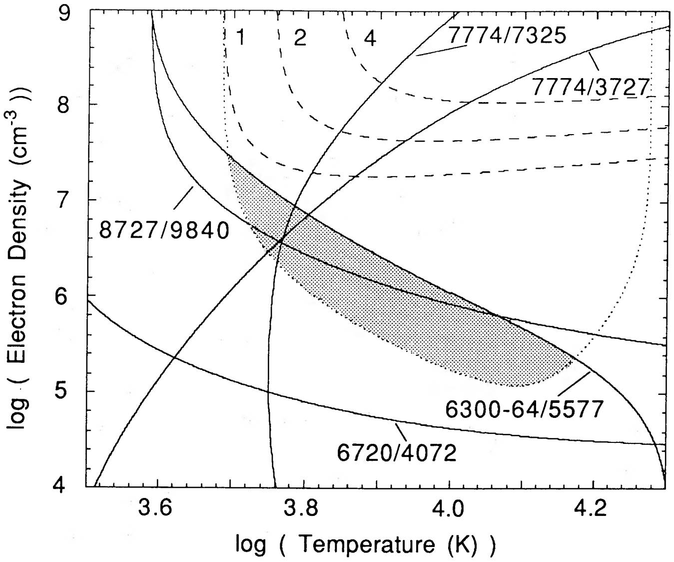

FIG. 11.—Density-temperature plane, indicating the allowed regions for the [O I] λλ6300, 6364/λ5577, O I λ7774/[O II] λ7325, O I λ7774/[O II] λ3727, [C I] λ8727/λ9840, and [S II] λ6720/λ4072 line ratio, observed for SN 1985F. The dashed lines gives the locus of the lines for a given total [O I] λλ6300, 6364 luminosity, in 10^{40} ergs s^{-1}, and for a total oxygen mass of 1 $M_\odot$. These assume that the O I and O II zones coincide. If this is *not* the case, the shaded region above the dotted line is allowed.

If the temperature-density region allowed in Figure 11 is compared with Figure 9, one sees that the Ca II H and K lines are expected to be weak, in agreement with the observations. If we identify the line at 7296 Å with [Ca II], the observed ratio of [Ca II] λ7300/[O I] λλ6300, 6364 ~ 0.3, together with Figure 9, indicates a relative abundance of Ca II/O I of ~(0.3–1.0) × 10^{-3}, by number, for T_e in the range 4000–7000 K and n_e greater than 10^6 cm^{-3}. Since both ions are the dominant ionization stages, this would also give the relative abundances. This estimate, however, assumes that the Ca II and O I regions coincide, which is far from obvious, and the ratio should thus be taken with considerable caution. The same argument can be used on the observations of SN 1987A.

In summary, we find that solely on this type of analysis the exploding white dwarf model *cannot* be excluded. Although this type of analysis may indicate the approximate physical conditions in the line-forming regions, it should be used with care. Both the nonuniform structure and the largely unknown ionization equilibrium can affect the results by large factors. Instead one has to use a more sophisticated self-consistent modeling as in § V, where more constraints from the ionization balance and radiative equilibrium are included. This will be discussed next.

© American Astronomical Society • Provided by the NASA Astrophysics Data System

1989ApJ...343..323F

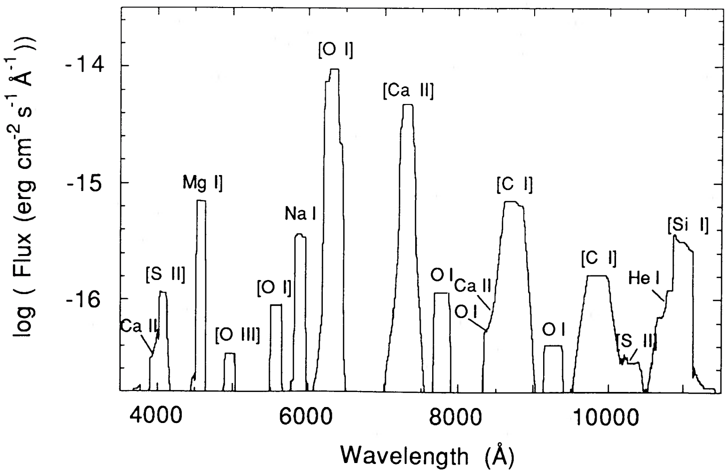

FIG. 12.—Synthetic spectrum for model 1b (8 $M_{\odot}$ He core) 300 days after the explosion. The expansion velocity of the O core was ~ 5140 km s^{-1}. Note that several lines, e.g., [O I] λλ6300, 6364 and Ca II λλ8498–8662 + [C I] λ8727, are blends. The large width of [C I] λλ9824, 9850 is mainly due to the contribution of the high-velocity He mantle.

b) Self-consistent Models of Massive Cores

To avoid the uncertainties connected with, e.g., the ionization equilibrium and nonuniform structure, one has to calculate a self-consistent model along the lines of § V. This is also the most natural way to test a given explosion model with the observations. For this we have calculated synthetic spectra, including the blending of the lines. This is in most cases trivial, since most forbidden and semiforbidden lines are optically thin. The different multiplet components are weighted according to their statistical weights and transition probabilities, as long as they are optically thin. In Figure 12 we show a spectrum, 300 days after the explosion, for the 8 $M_{\odot}$ He core (WW model 8B, ZAMS mass 25 $M_{\odot}$), model 1b. For a comparison with SN 1985F we assume a distance of 8 Mpc. The velocity at the O/He interface is ~ 5200 km s^{-1}, which determines the total line width. In Figures 7 and 8 the structure of this model at the same epoch is shown. It should be stressed that there are very few free parameters in these models, except for the core mass, the ^{56}Ni mass, and the core velocity, all strongly constrained by the observations. We have not attempted here to get a best-fit model by varying the density and abundance structure. Given this, there is a remarkably good *qualitative* agreement between the March/April spectrum in FS86 and Figure 12, in terms of both the lines present and their relative strengths. As noted by Filippenko and Sargent, their identifications are in some cases uncertain because of the widths of the lines, and the feature with a broad peak at 4036 Å is, e.g., consistent with [S I] λλ4069, 4076, within the errors. We note that most of the emission in the line at ~ 7296 Å is due to [Ca II] λλ7291, 7324, with only a small fraction from [O II] λλ7320, 7331. Most of the wide feature at 8700 Å is due to [C I] λ8727, with contributions of O I λ8446 and Ca II λλ8498–8662 in the blue wing. Also the strength of [C I] λλ9824, 9850 is well reproduced. The main discrepancy is in the Na I λ5890 strength, which is underestimated. This is, however, probably the most uncertain line, both in terms of the ionization balance and also in terms of the total Na abundance in the models. As discussed in § V*b*, all elements with low ionization potentials, like Na I, Mg I, and Si I, are sensitive to the diffuse emission between 5 and 11 eV. As for the relative strengths of the O I recombination lines at 7774, 8446, and 9264 Å, these agree well with the observations. This is expected, since optical depth effects are small and the line intensities are close to their recombination values, except at early epochs. The O I line at 6157 Å is weak and blended with the [O I] line wing, and the 11287 Å line outside the observed range. As shown in § III, there is a close correspondence between the observed O I λ7774/[O I] λλ6300, 6364 ratio and the ratio of the γ-ray energy going into ionizations and electron heating. The forbidden [Si I] lines at 1.099 and 1.645 μm are not in the range observed for this supernova, but the 1.6068–1.6455 μm lines were probably present in the IR spectra of the Type Ib SN 1983N observed by Graham *et al.* (1986) ~ 1 yr after the explosion. These authors attributed the line to the [Fe II] λλ1.600, 1.644, 1.664, 1.677 μm multiplet, but an equally likely interpretation, consistent with the expected strength, is due to the [Si I] line (Oliva 1987; Fransson 1987). The temperature where most of the [Si I] emission originates is ~ 3000 K, and the fraction in Si I is ~ 0.5. These values are considerably different from those assumed by Oliva (1987), decreasing the total amount of Si to $\sim 7 \times 10^{-2}$ $M_{\odot}$.

Although the He mantle was included in the calculations, there is, except for the IR 10830 Å line, little trace of He in the spectrum. Instead, most of the absorbed energy is in the optical emitted as [C I] λ8727, and [Ca II] λ7300. These lines therefore show a larger velocity width than lines coming solely from the core. For an unmixed remnant, the iron lines are expected to come from the inner core. The emission from this region has not been calculated in detail. but the total Fe I–Fe II emission is less than $\sim 20\%$ of the total. Part of the "continuum" seen in SN 1985F may be a result of this.

As is seen from models 4 and 5 in Table 2, a smaller core mass, 4–6 $M_{\odot}$, gives considerably worse agreement, both in absolute and relative line strengths. Especially the Ca II/[O I] and [C I]/[O I] ratios are inconsistent with the observations. Judging from these models, a He core mass of ~ 8 $M_{\odot}$, or somewhat higher, is needed for the Type Ib's. This means a ZAMS mass of ~ 25 $M_{\odot}$.

The main problem with these models is that the line profiles in Figure 12 are too flat, compared with the peaked profiles in the observed spectrum (e.g., Fig. 4 of FS85). This is a result of the shell structure in the hydrodynamical models, caused by

© American Astronomical Society • Provided by the NASA Astrophysics Data System

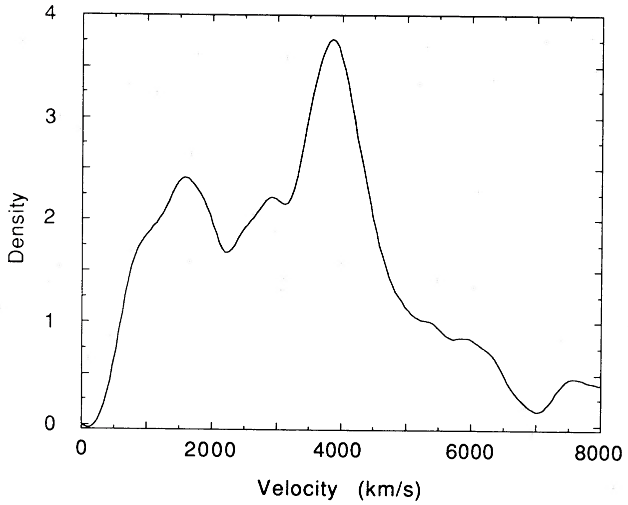

FIG. 13.—Density distribution of SN 1985F, as inferred from the blue wing of [O I] λ6300. The unit of the density scale is arbitrary, while the radius is given in velocity units [since $V(r) \propto r$].

TABLE 3

LUMINOSITIES AFTER 300 DAYS ILLUSTRATING THE EFFECT OF MIXING

Species	λ (Å)	Model M1	Model M2	Model 3
C I	8727	1.60	1.60	1.58
O I	6300, 6364	2.99	3.22	12.28
Na I	5890, 5896	1.08	1.08	0.13
Mg I	4571	0.78	0.98	0.38
Mg II	2796, 2803	2.07	0.76	4.84
Ca II	7291, 7324	22.8	24.4	9.31
Ca II	8498–8662	1.42	1.11	0.33
"Fe I"	...	1.25	0.38	6.20
"Fe II"	...	19.9	22.1	14.4

NOTE.—Model M1: totally mixed; model M2: totally mixed except for Fe; model 3: unmixed. All luminosities are in units of 10^{39} ergs s^{-1}.

the ^{56}Ni heating, with nearly all the mass at one velocity. To estimate the required distribution of the ejecta, we have applied equation (15) to the blue wing of [O I] λ6300 in the spectrum of SN 1985F (FS85). For SN 1985F the emission was dominated by [O I] λλ6300, 6364, so the line profile should reflect the total energy input, and thus the density distribution. For this analysis we have first subtracted the 6364 Å component, assuming a ratio λ6300/λ6364 equal to 3.0. We have then filtered out the noise and from this calculated a running derivative for segments of 15 Å (714 km s^{-1}), which represents the smoothing in velocity. In Figure 13 we show the density (or more precisely the function $\epsilon\, dI(\epsilon)/d\epsilon$, where ϵ is the relative shift in velocity from the line center) in arbitrary units as a function of the velocity, and thus of the radius ($V \propto r$). The accuracy of this curve is ~25% in the density, for velocities less than ~700 km s^{-1}. For higher velocities, the continuum level makes the line profile uncertain. Also at velocities below ~500 km s^{-1} at the peak of the line, the results are uncertain. Irrespective of this, however, *the observed density profile gives a much wider distribution than that obtained from the hydrodynamic models.* This is a rather firm conclusion, since the flat profile is simply the result of the absence of material at low velocities. Relaxing the assumption of a central γ-ray source will only give a less centrally peaked line profile. A likely explanation for this discrepancy is that hydrodynamic instabilities influence the density distribution. In particular, the radioactive heating may give rise to Rayleigh-Taylor instabilities. Also, the early expansion and the ingoing rarefaction wave may give rise to the same instability (Chevalier and Klein 1978). This could both lead to a mixing between different burning shells and leave material at low velocities.

If the line profiles of [O I] λ6300 and Mg I] λ4571 in FS85 are compared, it is found that they have very similar profiles. Both lines show a marked asymmetry, with the red wing considerably steeper than the blue. This is most likely an indication that the envelope is not spherically symmetric, or that continuous scattering within the envelope is important, since occultation effects at these epochs should be small. Also the blue widths of the lines are similar, except that the [O I] line has a faint wing above ~6000 km s^{-1}, extending up to ~15,000 km s^{-1} (FS85). As discussed above, the high-velocity wing may arise in the He mantle. The maximum velocities of the Mg I], Na I, [O I], [Ca II], and [C I] profiles in FS86 are all nearly the same, ~4500 km s^{-1}. This is surprising, since for an extended shell one expects the Mg I] emission to come mainly from the inner part of the oxygen region, and thus have a lower velocity. The same applies even more to Ca II. Therefore, both the density profile and the line widths indicate that mixing is important.

Since the density, and probably also element distribution, are quite different from those of the WW models, it is legitimate to ask how this may affect the synthetic spectrum. We have therefore calculated two models with constant O core density between 1000 and 5200 km s^{-1} and constant abundances throughout the shell, simulating the effect of a microscopic mixing. In one of the models the Fe abundance is also mixed (model M1) and in one it is unmixed (model M2). The effect of only changing the density, without mixing, can be seen in the constant-density unmixed model, model 3. In Table 3 we give the most important line luminosities for these three models at 300 days. Comparing the mixed models with the unmixed, one immediately notices the large increase in [Ca II] λλ7291, 7324 at the expense of [O I] λλ6300, 6364. The ratio of the two lines increases by a factor of ~10! This effect, due to the dominance of Ca II as a coolant, has already been discussed for the 15 $M_\odot$ models in § Vc. The decrease in the [O I] strength is directly compensated by a similar increase in the Ca II strengths, making the line ratio very sensitive to the relative Ca/O abundances in the O shell. The line profiles of the two models are, however, quite different. In model 3 the [Ca II] velocity is ~50% of the [O I] velocity, while in the mixed models the two velocities are the same. The emission from Fe II is also sensitive to mixing. The [C I] emission is less affected, since a large fraction is coming from the He mantle. These models illustrate that the late spectrum is very useful for the understanding of the mixing process both in the progenitor and in the explosion.

Summarizing, we therefore have a contradictory situation. The line profiles and widths indicate an extended density distribution with a mixing of the different burning zones. Such a homogeneous mixing, however, changes the spectrum drastically. For example, to reproduce the observed [Ca II]/[O I] ratio the Ca abundance has to be decreased by a factor ~20 relative to model 8B. This factor depends on the uncertain $4s\,^2S$–$3d\,^2D$ transition probability.

1989ApJ...343..323F

This problem, however, depends on the assumption of *microscopic* mixing. In the case of a lumpy structure with blobs of material from different burning shells mixed only *macroscopically*, the situation is quite different. The composition in the different components is then given not by an average but by the amount present in each burning zone. Therefore, the emission from each of these components is similar to that of the unmixed case. The total flux from each burning zone is then a function mainly of the mass fraction of each burning shell and the radial position (or velocity) of the shell. In the case of a geometrically uniform macroscopic mixing of all shells in the core, the flux from each component will be directly proportional to the component's mass. We think that such a *macroscopic mixing is a likely solution*, since this allows us to combine both the success of the unmixed model for the total emission and the reproduction of the observed line profiles. A quantitative verification of this is obviously difficult, since it depends on the calculation of a highly inhomogeneous distribution. A first approximation may, however, be a simple addition of weighted contributions from the various shells. Since conductivity is not likely to be important, one can expect widely different temperatures of these components, especially if the blobs are close to the temperature where the thermal instability sets in.

There is evidence for a similar macroscopic mixing from other sources. Thus, in the Cas A remnant there is a lack of correlation in velocity between the fast-moving knots coming from different nuclear burning zones (Chevalier and Kirshner 1979). Also, from the X-ray and γ-ray observations of SN 1987A there is evidence for macroscopic mixing of Fe group elements in the core (e.g., Shibazaki and Ebisuzaki 1988). A homogeneous mixing would also lead to a complete dominance of Fe II emission in the optical spectrum. Arnett (1988) has also stressed that microscopic mixing is inefficient and that macroscopic mixing is important for the light curve of SN 1987A.

c) Exploding White Dwarfs

White dwarf models have been suggested for the Type Ib supernovae (Branch and Nomoto 1986; Woosley 1986). Branch (1988) has argued that these in principle can fulfill the observational requirements for the radio emission, the connection with H II regions, and the light curves. We will thus here discuss what we expect in terms of the late spectrum for this type of object. Models of exploding white dwarfs have been calculated by several groups (see Nomoto 1984 and Woosley and Weaver 1986 for reviews). The general feature of these models is that they produce 0.6–1.4 $M_\odot$ of Fe-like nuclei, most in the form of ^{56}Ni. The rest of the mass is in the form of partially incinerated nuclei of Ne-Ca, some oxygen resulting from carbon burning, and unburned carbon and oxygen. From spectral modeling of the standard Type Ia supernova SN 1981B, Branch *et al.* (1985) found that good agreement could be obtained with a model, W7 (Nomoto, Thielemann, and Yokoi 1984), where 0.82 $M_\odot$ has been burned to nuclear statistical equilibrium and only $\sim$0.5 $M_\odot$ of C-Ca elements are present. The best agreement was found for a model where the outer layers were strongly mixed, possibly because of large-scale mixing (Müller and Arnett 1985). Of the partially burned material, only 0.14 $M_\odot$ was in the form of ^{16}O. This amount is far too small to reproduce the observed properties of the Type Ib supernovae, and the Co-Fe models for ordinary Type I's of Axelrod (1980*a*, *b*) are more appropriate.

The relative strengths of the lines from low- and intermediate-mass elements to those from Fe and Co can be estimated from the ratio of the optical depths to the γ-rays of the two regions. We find that for the C6 and W7 models this ratio is $\sim$0.15 and $\sim$0.08, respectively. Therefore, these spectra are dominated by Fe/Co emission. The maximum non-Fe contribution relative to Fe/Co is obtained if all the iron is concentrated in a narrow shell at the boundary of the two regions, and immediately outside of this the non-Fe elements. In this case, the optical depths, and thus the relative line strengths, are just given by the ratio of their masses, M(non-Fe)/M(Fe-Co). The model proposed by Branch and Nomoto (1986) for Type Ib's differs in that the ^{56}Ni source is outside the C/O region. This means that only one-half of the γ-rays pass through the C/O region. Of these, a fraction $\langle \tau_\gamma \rangle$ will be absorbed, where

$$\langle \tau_\gamma \rangle = \kappa_\gamma R \int_0^1 \int_{(1-\mu^2)^{1/2}}^1 \frac{\rho(l(x)/R)x}{[x^2 - (1-\mu^2)]^{1/2}}\, dx\, d\mu \quad (18)$$

and $l(x)/R = \{\mu + [x^2 - (1-\mu^2)]^{1/2}\}$. The maximum occurs for a thin C/O shell inside the ^{56}Ni region with a total

$$\langle \tau_\gamma \rangle_{\max} = \frac{2\kappa_\gamma M_{\rm CO}}{4\pi R^2} = 2.9 \times 10^{-2}\left(\frac{M_{\rm CO}}{M_\odot}\right) \times \left(\frac{V_c}{5000 \text{ km s}^{-1}}\right)^{-2}\left(\frac{t}{300 \text{ days}}\right)^{-2} . \quad (19)$$

Here $M_{\rm CO}$ is the mass of the C/O region. Therefore, the γ-ray energy absorbed will be

$$L_\gamma \lesssim 2.8 \times 10^{40}\left[\frac{M(^{56}\text{Ni})}{M_\odot}\right]\left(\frac{M_{\rm CO}}{M_\odot}\right)\left(\frac{V_c}{5000\,\text{km s}^{-1}}\right)^{-2} \times \left(\frac{t}{300 \text{ days}}\right)^{-2} \exp\left(-\frac{t-300}{114}\right) \text{ergs s}^{-1} . \quad (20)$$

For equal C/O and ^{56}Ni masses, 0.7 $M_\odot$, the total absorbed energy is thus $\sim 1.4 \times 10^{40}$ ergs s^{-1} at 300 days. This is less than the energy in *only* the [O I] line in SN 1985F, and this model thus meets large difficulties in explaining the energy emitted.

The degree of burning, and thus also the ratio of Fe group elements to intermediate- and low-mass elements, is sensitive to the detailed physics of the carbon deflagration front. Since the treatment of this is fairly approximate, the extent of the burning may be considered as a free parameter. For an explosion to occur, the released nuclear energy, however, has to exceed the binding mass of the white dwarf, which corresponds to 5×10^{50} ergs. Thus, at least 0.16 $M_\odot$ of ^{56}Ni and 0.2 $M_\odot$ of other elements must be produced to overcome this barrier (Arnett, Branch, and Wheeler 1985). To give the ejecta a velocity of $\sim 10^4$ km s^{-1} Arnett *et al.* estimate that $\sim$0.4 $M_\odot$ of ^{56}Ni must be produced, together with $\sim$0.4 $M_\odot$ of other elements, leaving $\sim$0.6 $M_\odot$ of unburned C/O. As a "most optimistic case," we have taken a model provided by Woosley (1986), where the deflagration wave died after having burned only $\sim$0.2 $M_\odot$ of ^{56}Ni, a total "Fe group" mass of 0.4 $M_\odot$, 5.8×10^{-2} $M_\odot$ of Ne-Ca elements, and 0.94 $M_\odot$ of C + O. The relative fraction of C/O was 0.96:1 by mass, but it reflects mainly the assumption of an initial 1:1 ratio, since the nuclear burning in the supernova only affects the oxygen mass slightly.

© American Astronomical Society • Provided by the NASA Astrophysics Data System

The density in the supernova is in the outer parts close to that of the initial $n = 3$ polytrope. As for the massive cores, the heating by the γ-rays and the compression by the deflagration wave results in a central low-density region and a peak between ~ 0.45 and ~ 0.65 $M_\odot$, coinciding with the transition between the incinerated core and the C/O region. The density increase is a factor of ~ 4, compared with the initial distribution. In Table 2 we give the resulting line luminosities for this model 200 and 300 days after the explosion as models 6a and 6b. The γ-ray optical depths of these models are 0.23 and 0.10, respectively, which is the fraction of the γ-ray luminosity emitted as optical line emission. In the central Co-Fe region, $m(r) \leq 0.4$ $M_\odot$, ions of these elements also dominate the line emission, as calculated in detail by Axelrod (1980*b*). This accounts for $\sim 42\%$ of the total emission, close to the relative fraction of the γ-ray optical depth of the Fe-region, $\Delta\tau_\gamma = 0.13$. The optical depth of the outer "non-Fe" regions is 0.10 (both at 200 days). In a thin shell between 0.4 and 0.6 $M_\odot$, there is a mixture of intermediate-mass elements. The cooling is dominated by lines from elements of the Mg-Ca group, with Mg I] λ4571, Na I $\lambda\lambda$5890, 5896, and [Ca II] λ7300 as the most important. The region outside ~ 0.4 $M_\odot$ consists of mainly unburned C and O, and the emission is dominated by [C I] $\lambda\lambda$2967, 8727, 9824, 9850, C II] λ2326, and [O I] $\lambda\lambda$6300, 6364. While the ratio of the 5577 Å to the 6300, 6364 Å lines, 1/15, is probably acceptable, the luminosity of the [O I] $\lambda\lambda$6300, 6364 line is small by a factor of at least 2, even at 200 days. At 300 days it is down by an order of magnitude. However, perhaps the most interesting aspect, and *a characteristic feature of the white dwarf models, is the high* [C I] λ8729/[O I] $\lambda\lambda$6300, 6364 *ratio*. At 200 days the ratio is 1.9, and at 300 days it is 0.94. This is in contradiction to the observations of SN 1985F, where the ratio is <0.17 (FS86). It may be argued that the C:O ratio could be considerably lower than that assumed in this model, and we have therefore also calculated two models with C:O ratios of 2:8 and 1:9, but otherwise the same structure as model 6. At 200 days the former has a [C I] λ8727/[O I] $\lambda\lambda$6300, 6364 ratio of 0.46, and the latter a ratio of 0.21, still higher than the observed. It should also be pointed out that the ionization equilibrium of both C and O are insensitive to photoionization, and should be fairly accurate. From this point of view it is unlikely that this model applies to the Type Ib supernovae, unless C/O is less than ~ 0.1. This argument does not apply to the massive cores, since in these the carbon region is generally outside of the oxygen shell, with a smaller column density.

Model 6 is in many respects a most optimistic white dwarf case for the Type Ib scenario, involving a maximum oxygen mass. In addition, there is no mixing of the Fe or Si-Ca regions with the C-O shell. Any such mixing, which is likely to occur as a result of instabilities, will decrease the C I and O I fluxes while increasing those of Mg, Ca II, and Fe (§§ V*c* and VI*b*). This, as well as the argument about the [C I]/[O I] ratio and the small [O I] $\lambda\lambda$6300, 6364 luminosity, also apply to the model by Branch and Nomoto (1986). Another severe problem with model 6 is that the line profiles are flat out to ~ 3900 km s^{-1}.

VII. CONCLUSIONS

In this paper we have discussed the general physics of a supernova envelope dominated by energy input from γ-rays. The general method and input physics may serve as the starting point for future modeling, especially of SN 1987A. Although many uncertainties remain to be resolved, we think that the results here show that it will be feasible in the future to understand the nucleosynthetic process of massive stars from the late spectra. This can be approached from either of two directions. In the first, one can from the density and nucleosynthetic structure of a given hydrodynamical model calculate the resulting emission spectrum, which can then be compared with the observations to test the model. That this approach is already realistic has been demonstrated in §§ VI*b* and VI*c*. In the other, more ambitious approach, one can use this type of model as a diagnostic tool, and directly from the observations in an iterative procedure derive both abundances and the density distribution. A simple version of this method, discussed in § VI*a*, uses only the total line strengths in a classical nebular analysis. This may, however, lead to large errors due to an inhomogeneous structure. Another problem is that the relative fraction of a given ion to the total abundance is usually unknown. As we have shown in §§ IV and VI*b*, for both of these approaches the line profile contains crucial information for the determination of both the element distribution and the total density. Unfortunately, this has not been used much before. For future supernovae, medium-resolution observations (~ 2 Å) of high S/N are highly desirable, in order to get reliable line profiles at late times. As Filippenko and Sargent (1985) have demonstrated, this is well within current capabilities, even for quite faint supernovae.

In this paper we have applied our model to the Type Ib supernovae to compare the observations with current nucleosynthesis models. The models have already been used to discuss possible scenarios for the late core emission of Type II's, with special emphasis on SN 1987A (Fransson and Chevalier 1987; Fransson 1987, 1988). The models in this paper, based on the core emission from exploding massive stars, are fairly successful in reproducing both the absolute luminosities and the relative fluxes of the lines present in the Type Ib's. This may conflict with the conclusions from the light-curve calculations by Ensman and Woosley (1988). However, the severe disagreement between the observed line profiles and those resulting from the hydrodynamical models shows that there are many uncertainties in the hydrodynamical models. The problems include the effects of instabilities, mixing, and nonspherical distortions. We have argued that a macroscopic mixing of blobs from the different burning shells may explain the peaked line profiles. At the same time, this will preserve the agreement of the relative fluxes from the unmixed models. If the remnant consists of blobs and filaments of varying density and composition, the temperature and ionization may vary considerably between elements close to each other. Also the thermal instability triggered by the IR cooling may set in at different epochs in different blobs, depending on the density and composition. This may further enhance the inhomogeneous structure of the remnant.

The presence of a pulsar may be important after about 2 years, when the radioactivity has decayed. A pulsar will be surrounded by a plerionic synchrotron nebula, emitting ionizing radiation. The ejecta will thus be gradually ionized as they expand. In contrast to the γ-ray–heated case, most of the absorbed energy is expected to be emitted as lines of highly ionized elements in the UV. These issues are further discussed in Fransson and Chevalier (1987) and Fransson (1987). The energy input from the pulsar may also prevent the thermal instability from occurring. Chevalier (1987) has proposed that the optical emission from SN 1986J (Rupen *et al.* 1987) may be the result of pulsar excitation.

We are grateful to Alexei Filippenko for providing the original data on SN 1985F, to Stan Woosley and Lisa Ensman for sending their explosion models, and to Claes-Ingvar Björnsson and Phil Pinto for discussions. The research of R. A. C. is supported in part by National Science Foundation grant AST-8615555 and by National Aeronautics and Space Administration grant NAGW-764.

APPENDIX A

ATOMIC DATA: NONTHERMAL PROCESSES

To study the deposition of the nontherma electrons in the different channels, we include for oxygen both excitations to discrete levels, ionizations to the continua of O II and O III, and Coulomb heating of the thermal electrons. The levels included are the same as for the multilevel atom shown in Figure 4. For the electron impact excitation from the ground state ^3P to $2p\ ^1D$ and $2p\ ^1S$ we use the cross sections from Berrington, Burke, and Robb (1975); to $3s\ ^3S^o$, $3s\ ^5S^o$, and $3p\ ^5P$ from Smith (1976); to $3p\ ^3P$ from Sawada and Ganas (1973); and to $3d\ ^3D$ from Kazaks, Ganas, and Green (1972). The ionization cross section for O I was taken from Brook, Harrison, and Smith (1978), and for O II from Lotz (1967). Also, for He I and Ca II we take the most important discrete excitations into account. For He I, the $2s\ ^3P$ and $2p\ ^1P$ levels are included with cross sections from Jobe and St. John (1967), and for Ca II the H and K resonance transition, with a cross section taken from Kennedy, Myerscough, and McDowell (1977). For the other elements we neglect discrete excitation, which, as shown by the O I calculations, is a good approximation for $x_e > 0.1$. Ionization cross sections for He I, Na I, Mg II, Si I, Ca I, and Ca II are obtained from Lotz (1967, 1968); for C I from Brook, Harrison, and Smith (1978); for Mg I from Karstensen and Schneider (1978); and for S I from Ziegler *et al.* (1982).

For the energy transfer rate between the thermal, free electrons and the nonthermal electrons we use the expression given by Schunk and Hays (1971). The energy step size was set to $\Delta E/E = 0.05$ (Shull 1979). For the energy distribution of the secondary electrons emitted by the ionizations, the results of Opal, Peterson, and Beaty (1971) are used for He I, O I, Ne I, and Ar I. For other ions no experimental results are available, and we assume that the distributions are the same, scaled according to the ionization potentials. The results are not sensitive to these assumptions.

APPENDIX B

THERMAL RATES

Collisional excitation rates and transition probabilities for both electronic and fine-structure transitions are taken mainly from the compilation of Mendoza (1983), unless stated otherwise. For C II λλ1334, 2326 and C II λ158 μm, data are from Hayes and Nussbaumer (1984). Collisional excitation of Na I is from Kennedy, Myerscough, and McDowell (1977), and for Mg I] λλ2853, 4571 from Fabrikant (1974). For [Si I] ^3P–^1D we use a rate based on Pindzola, Bhatia, and Temkin (1977), which is, however, uncertain by a factor of 2. For [Si I] ^1D–^1S and ^3P–^1S no collisional strengths are available at all, and we instead use those of [O I]. The [Si I] λ1.099 μm strength is thus especially uncertain. For the fine-structure transitions where collision strengths are not available ([C I], [Si I], [Si II], and [S I]), rates for ions with similar electronic configurations are used. Since the fine-structure levels are close to LTE, the collision rates are not critical.

Photoionization cross sections are taken from Reilman and Manson (1979), except for Na I (Butler and Mendoza 1983) and Ca I (Scott, Kingston, and Hibbert 1983). Collisional ionization rates by thermal electrons are from Shull and van Steenberg (1982). Radiative and dielectronic recombination rates are from Gould (1978), Aldrovandi and Péquignot (1973, 1974), Woods, Shull, and Sarazin (1981), and the low-temperature dielectronic rates are from Nussbaumer and Storey (1984, 1986). Charge transfer between especially the abundant ions, such as O I and O II, and the trace elements, such as Mg, Na, and Ca, can be equally as important as or more important than the radiative ionization and recombination rates. Unfortunately, rates of many of these reactions are lacking, or only weak upper limits are available. An important example is Ca I($^1S_0$) + O II($^4S^o$) → Ca II($5p\ ^2P_{1/2}$) + O I(^3P) (see § V*b*), with a rate of 2.09×10^{-9} cm^3 s^{-1} at 1200 K (Rutherford *et al.* 1972*b*). This scales roughly as $T_e^{1/2}$. For the reactions Na I + O II → Na II + O I and Mg I + O II → Mg II + O I only upper limits exists (Rutherford *et al.* 1972*a*, 1971).

For the multilevel calculation of O I we include the levels and transitions shown in Figure 4. Transition probabilities are from Mendoza (1983), Christenson and Cunningham (1978), Wiese, Smith, and Glennon (1966), and Wiese and Martin (1980). For the forbidden lines we use collisional excitation rates from Mendoza (1983), and for the excited states rates based on the cross sections in Appendix A, or where these are lacking, the van Regemorter formula. Collisional ionization rates from the excited and ground states are from Summers (1974). Photoionization rates from the ground state are from Henry (1970), and those from the excited states are from Davis and Lewis (1973). The O I recombination rates to excited levels are calculated from the photoionization cross sections above, or, for the levels not explicitly included in the model atom, are taken from Julienne, Davis, and Oran (1974).

In the He I atom we include singlet levels up to $2\ ^1P$ and triplet levels up to $4\ ^3F$. Transition rates are from Wiese, Smith, and Glennon (1966) and MacAlpine (1976), collisional excitation rates from Berrington *et al.* (1985) and Feldman and MacAlpine (1978), effective recombination rates from Osterbrock (1974), and collisional ionization rates from Mihalas and Stone (1968).

For Ca II we include the $4s\ ^2S$, $3d\ ^2D$, $4p\ ^2P^o$ states, plus the continuum. Collisional rates, photoionization cross sections, and transition probabilities are from Shine and Linsky (1974), except for the important forbidden transition at 7291, 7324 Å, where the transition probability is obtained from Wiese, Smith, and Glennon (1966). Unfortunately, the latter is probably rather uncertain.

© American Astronomical Society • Provided by the NASA Astrophysics Data System

1989ApJ...343..323F

REFERENCES

Ahlen, S. P. 1980, *Rev. Mod. Phys.*, **52**, 121.
Aldrovandi, S. M. V., and Péquignot, D. 1973, *Astr. Ap.*, **25**, 137.
———. 1974, *Rev. Brasileira Fis.*, **4**, 491.
Arnett, W. D. 1988, in *SN 1987A in the Large Magellanic Cloud*, ed. M. Kafatos and A. Michalitsianos (Cambridge: Cambridge University Press), p. 301.
Arnett, W. D., Branch, D., and Wheeler, J. C. 1985, *Nature*, **314**, 337.
Axelrod, T. S. 1980*a*, in *Type I Supernovae*, ed. J. C. Wheeler (Austin: University of Texas Press), p. 80.
———. 1980*b*, Ph.D. thesis, University of California, Santa Cruz.
Barbon, R., Cappellaro, E., and Turatto, M. 1984, *Astr. Ap.*, **135**, 27.
Barbon, R., Ciatti, F., and Rosino, L. 1982, *Astr. Ap.*, **116**, 35.
Barbon, R., Ciatti, F., Rosino, L., Ortolani, S., and Rafanelli, P. 1982, *Astr. Ap.*, **116**, 43.
Begelman, M. C., and Sarazin, C. L. 1986, *Ap. J.* (*Letters*), **302**, L59 (BS).
Berrington, K. A., Burke, P. G., Freitas, L. C. G., and Kingston, A. E. 1985, *J. Phys. B*, **18**, 4135.
Berrington, K. A., Burke, P. G., and Robb, W. D. 1975, *J. Phys. B*, **8**, 2500.
Branch, D. 1984, *Ann. NY Acad. Sci.*, **422**, 186.
———. 1988, in *IAU Colloquium 108, Atmospheric Diagnostics of Stellar Evolution: Chemical Peculiarity, Mass Loss, and Explosion*, ed. K. Nomoto (Springer Lecture Notes in Physics, Berlin: Springer), p. 281.
Branch, D., Doggett, J. B., Nomoto, K., and Thielemann, F.-K. 1985, *Ap. J.*, **294**, 619.
Branch, D., and Nomoto, K. 1986, *Astr. Ap.*, **164**, L13.
Brook, E., Harrison, M. F. A., and Smith, A. C. H. 1978, *J. Phys. B*, **11**, 3115.
Butler, K., and Mendoza, C. 1983, *J. Phys.* B, **16**, L707.
Cashwell, E. D., and Everett, C. J. 1959, *A Practical Manual on the Monte Carlo Method for Random Walk Problems* (New York: Pergamon).
Chevalier, R. A. 1976, *Ap. J.*, **207**, 872.
———. 1986, in *Highlights Astr.*, ed. J. P. Swings (Dordrecht: Reidel), p. 599.
———. 1987, *Nature*, **329**, 611.
Chevalier, R. A., and Kirshner, R. P. 1979, *Ap. J.*, **233**, 154.
Chevalier, R. A., and Klein, R. I. 1978, *Ap. J.*, **219**, 994.
Christenson, A. B., and Cunningham, A. J. 1978, *J. Geophys. Res.*, **83**, 4393.
Chugai, N. N. 1988, *Ap. Space Sci.*, **146**, 375.
Colgate, S. A., and McKee, C. 1969, *Ap. J.*, **157**, 623.
Colgate, S. A., Petschek, A. G., and Kriese, J. T. 1980, *Ap. J.* (*Letters*), **237**, L81.
Dalgarno, A., and Lejeune, G. 1971, *Planet. Space Sci.*, **19**, 1653.
Davis, J., and Lewis, J. 1973, *J. Quant. Spectrosc. Rad. Transf.*, **13**, 871.
Ensman, L. M., and Woosley, S. E. 1988, *Ap. J.*, **33**, 754.
Fabrikant, I. I. 1974, *J. Phys. B*, **7**, 91.
Feldman, F. R., and MacAlpine, G. M. 1978, *Ap. J.*, **221**, 486.
Filippenko, A. V. 1988, in *SN 1987A in the Large Magellanic Cloud*, ed. M. Kafatos and A. Michalitsianos (Cambridge: Cambridge University Press), p. 108.
Filippenko, A. V., and Sargent, W. L. W. 1985, *Nature*, **316**, 407 (FS85).
———. 1986, *A.J.*, **91**, 692 (FS86).
Fransson, C. 1986, in *Highlights Astr.*, ed. J. P. Swings (Dordrecht: Reidel), p. 611.
———. 1987, in *ESO Workshop on SN 1987A*, ed. I. J. Danziger (Garching: ESO), p. 467.
———. 1988, in *IAU Colloquium 108, Atmospheric Diagnostics of Stellar Evolution: Chemical Peculiarity, Mass Loss, and Explosion*, ed. K. Nomoto (Springer Lecture Notes in Physics), p. 383.
Fransson, C., and Chevalier, R. A. 1987, *Ap. J.* (*Letters*), **322**, L15.
Fransson, C., Grewing, M., Cassatella, A., Panagia, N., and Wamsteker, W. 1987, *Astr. Ap.*, **177**, L33.
Gaskell, C. M., Cappellaro, E., Dinerstein, H. L., Garnett, D. R., Harkness, R. P., and Wheeler, J. C. 1986, *Ap. J.* (*Letters*), **306**, L77.
Gould, R. J. 1978, *Ap. J.*, **219**, 250.
Graham, J. R., Meikle, P. S., Allen, D. A., Longmore, A. J., and Williams, P. M. 1986, *M.N.R.A.S.*, **218**, 93.
Harkness, R. P., *et al.* 1987, *Ap. J.*, **317**, 355.
Hayes, M. A., and Nussbaumer, H. 1984, *Astr. Ap.*, **134**, 193.
Henry, R. J. W. 1970, *Ap. J.*, **161**, 1153.
Hummer, D. G., and Rybicki, G. B. 1985, *Ap. J.*, **293**, 258.
Iben, I., Jr., Nomoto, K., Tornambé, A., and Tutukov, A. V. 1987, *Ap. J.*, **317**, 717.
Jobe, J. D., and St. John, R. M. 1967, *Phys. Rev.*, **164**, 117.
Julienne, P. S., Davis, J., and Oran, E. 1974, *J. Geophys. Res.*, **79**, 2540.
Karstensen, F., and Schneider, M. 1978, *J. Phys. B*, **11**, 167.
Kazaks, P. A., Ganas, P. S., and Green, A. E. S. 1972, *Phys. Rev. A*, **6**, 2169.
Kennedy, J. V., Myerscough, V. P., and McDowell, M. R. C. 1977, *J. Phys. B*, **10**, 3759.
Kirshner, R. P., and Oke, J. B. 1975, *Ap. J.*, **200**, 574.
Lotz, W. 1967, *Ap. J. Suppl.*, **14**, 207.
Lotz, W. 1968, *Zs. Phys.*, **216**, 241.
Lucy, L. B. 1987, *Astr. Ap.*, **182**, L31.
MacAlpine, G. M. 1976, *Ap. J.*, **204**, 694.
McGregor, P. J., and Hyland, A. R. 1987, *IAU Circ.*, No. 4486.
Mendoza, C. 1983, in *IAU Symposium 103, Planetary Nebulae*, ed. D. R. Flower (Dordrecht: Reidel), p. 143.
Meyerott, R. E. 1980, *Ap. J.*, **239**, 257.
Mihalas, D., and Stone, E. S. 1968, *Ap. J.*, **151**, 293.
Müller, E., and Arnett, W. D. 1985, in *Nucleosynthesis: Challenges and New Developments*, ed. W. D. Arnett and J. W. Truran (Chicago: University of Chicago Press), p. 235.
Nomoto, K. 1984, in *Stellar Nucleosynthesis*, ed. C. Chiosi and A. Renzini (Dordrecht: Reidel), p. 205.
Nomoto, K., Shigeyama, T., and Hashimoto, M. 1987, in *ESO Workshop on SN 1987A*, ed. I. J. Danziger (Garching: ESO), p. 325.
Nomoto, K., Thielemann, F.-K., and Yokoi, K. 1984, *Ap. J.*, **268**, 644.
Nordlund, Å. 1984, in *Methods of Radiative Transfer*, ed. W. Kalkhofen (Cambridge: Cambridge University Press), p. 211.
Nussbaumer, H., and Storey, P. J. 1984, *Astr. Ap. Suppl.*, **56**, 293.
———. 1986, *Astr. Ap. Suppl.*, **64**, 545.
Oliva, E. 1987, *Ap. J.* (*Letters*), **321**, L45.
Opal, C. B., Peterson, W. K., and Beaty, E. C. 1971, *J. Chem. Phys.*, **55**, 4100.
Osterbrock, D. E. 1974, *Astrophysics of Gaseous Nebulae* (San Franscisco: Freeman).
Panagia, N. 1987, in *High Energy Phenomena around Collapsed Stars*, ed. F. Pacini (Dordrecht: Reidel), p. 33.
Panagia, N., *et al.*, 1989, in preparation.
Pindzola, M. S., Bhatia, A. K., and Temkin, A. 1977, *Phys. Rev. A*, **15**, 35.
Reilman, R. F., and Manson, S. T. 1979, *Ap. J. Suppl.*, **40**, 815.
Rohrlich, F., and Carlson, B. C. 1954, *Phys. Rev.*, **93**, 38.
Rupen, M. P., van Gorkom, J. H., Knapp, G. R., Gunn, J. E., and Schneider, D. P. 1987, *A.J.*, **94**, 61.
Rutherford, J. A., Mathis, R. F., Turner, B. R., and Vroom, D. A. 1971, *J. Chem. Phys.*, **55**, 3785.
———. 1972*a*, *J. Chem. Phys.*, **56**, 4654.
———. 1972*b*, *J. Chem. Phys.*, **57**, 3087.
Sawada, T., and Ganas, P. S. 1973, *Phys. Rev. A*, **7**, 617.
Schaeffer, R., Cassé, M., and Cahen, S. 1987, *Ap. J.* (*Letters*), **316**, L31.
Scharmer, G. B. 1987, private communication.
Schlegel, E. M., and Kirshner, R. P. 1989, preprint.
Schunk, R. W., and Hays, P. B. 1971, *Planet. Space Sci.*, **19**, 113.
Scott, P., Kingston, A. E., and Hibbert, A. 1983, *J. Phys. B*, **16**, 3945.
Shibazaki, N., and Ebisuzaki, T. 1988, *Ap. J.* (*Letters*), **327**, L9.
Shine, R. D., and Linsky, J. L. 1974, *Solar Phys.*, **39**, 49.
Shull, J. M. 1979, *Ap. J.*, **234**, 761.
Shull, J. M., and van Steenberg, M. 1982, *Ap. J. Suppl.*, **48**, 95.
Smith, E. R. 1976, *Phys. Rev.*, *A*, **13**, 65.
Spitzer, L., and Scott, E. H. 1969, *Ap. J.*, **158**, 161.
Spitzer, L., and Tomasko, M. G. 1968, *Ap. J.*, **152**, 971.
Spyromilio, J., Meikle, W. P. S., Learner, R. C. M., and Allen, D. A. 1988, *Nature*, **334**, 327.
Summers, H. P. 1974, Appleton Lab. Ap. Res. Div., Internal Rept., No. 367.
Sutherland, P. G., and Wheeler, J. C. 1984, *Ap. J.*, **280**, 282.
Tsvetkov, D. Yu. 1986, *Soviet Astr. Letters*, **12**, 328.
Uomoto, A., and Kirshner, R. P. 1986, *Ap. J.*, **308**, 685.
Weaver, T. A., Axelrod, T. S., and Woosley, S. E. 1980, in *Type I Supernovae*, ed. J. C. Wheeler (Austin: University of Texas Press), p. 113.
Weaver, T. A., and Woosley, S. E. 1980, in *Supernova Spectra*, ed. R. Meyerott and G. H. Gillespie (New York: AIP), p. 15.
Wheeler, J. C., Harkness, R. P., Barker, E. S., Cochran, A. L., Wills, B. J., and Wills, D. 1987, *Ap. J.* (*Letters*), **313**, L69.
Wheeler, J. C., and Levreault, R. 1985, *Ap. J.* (*Letters*), **294**, L17.
Wiese, W. L., and Martin, G. A. 1980, *Wavelengths and Transition Probabilities for Atoms and Atomic Ions*, Part 2 (Washington, DC: NBS).
Wiese, W. L., Smith, M. W., and Glennon, B. M. 1966, *Atomic Transition Probabilities* (NSRDS–NBS, Vol. **4**).
Woods, D. T., Shull, J. M., and Sarazin, C. L. 1981, *Ap. J.*, **249**, 399.
Woosley, S. E. 1986, talk presented at the 13th Texas Conference on Relativistic Astrophysics, (Chicago).
———. 1988, *Ap. J.*, **330**, 218.
Woosley, S. E., Taam, R. E., and Weaver, T. A. 1986, *Ap. J.*, **301**, 601.
Woosley, S. E., and Weaver, T. A. 1986, in *Radiation Hydrodynamics in Stars and Compact Objects*, ed. D. Mihalas and K. H. Winkler (Berlin: Springer), p. 91.
———. 1987, preprint (WW).
Ziegler, D. L., Newman, J. H., Goeller, L. N., Smith, K. A., and Stebbings, R. F. 1982, *Planet. Space Sci.*, **30**, 1269.

ROGER A. CHEVALIER: Department of Astronomy, University of Virginia, P.O. Box 3818, University Station, Charlottesville, VA 22903-0818

CLAES FRANSSON: Stockholm Observatory, S-133 00 Saltsjöbaden, Sweden

© American Astronomical Society • Provided by the NASA Astrophysics Data System